Advanced Materials

Multi-responsive Graphene Aerogel-directed Phase Change Smart Fibres

--Manuscript Draft--

Manuscript Number:	adma.201801754R2
Full Title:	Multi-responsive Graphene Aerogel-directed Phase Change Smart Fibres
Article Type:	Communication
Section/Category:	
Keywords:	graphene aerogel; smart fibre; Phase change materials; electrical/thermal/optical stimuli
Corresponding Author:	Xuetong Zhang Suzhou Institute of Nano-tech and Nano-bionics CHINA
Additional Information:	
Question	**Response**
Please submit a plain text version of your cover letter here. **If you are submitting a revision of your manuscript, please do not overwrite your original cover letter. There is an opportunity for you to provide your responses to the reviewers later; please do not add them here**.	March 19, 2018 Dear Editor, We would like to submit the enclosed manuscript entitled “Multi-responsive Graphene Aerogel-directed Phase Change Smart Fibres”, which was considered for publication in “Advanced Materials” as a research communication. Wearable devices and systems demand multifunctional units with intelligent and integrative functions. Smart fibres with response to external stimuli, such as electrical, thermal and photonic signals etc., as well as offering energy storage/conversion, are essential units for wearable electronics, but still remains great challenges. In this work, the flexible, strong and self-cleaning graphene aerogel composite fibres, with tunable functions of thermal conversion and storage under multi-stimuli, have been fabricated. The fibres made from porous graphene aerogel/organic phase change materials coated with hydrophobic fluorocarbon resin, rendered a wide range of phase transition temperature and enthalpy (0-186 J/g). The strong and compliant fibres were twisted into yarn and woven into fabrics, showing a self-clean super-hydrophobic surface and excellent multiple responsive properties to external stimuli (electron/photon/thermal) together with reversible energy storage and conversion. Such aerogel-directed smart fibres promise for broad applications in the next-generation of wearable systems. The significances of this work could be highlighted as follow: ★A new type of phase change fibers with the highest enthalpy has been reported in this manuscript ★The first multi-responsive phase change fibers with response to external stimuli, such as electrical, thermal and photonic signals etc., have been successfully fabricated. ★The first self-cleaning phase change fibers have been reported. ★The resulting phase change smart fibers could be twisted into yarn and woven into fabrics showing reversible energy storage and conversion. The work described has not been submitted elsewhere for publication, and all the authors listed have approved the manuscript that is enclosed. We would be grateful if the manuscript could be reviewed and considered for publication in Advanced Materials. Sincerely Yours, Xuetong Zhang ************************************** Prof. & Dr. Xuetong Zhang Suzhou Institute of Nano-Tech and Nano-Bionics, Chinese Academy of Sciences, Suzhou, 215123, P. R. China. E-mail: xtzhang2013@sinano.ac.cn **************************************

Do you or any of your co-authors have a conflict of interest to declare?	No. The authors declare no conflict of interest.
Corresponding Author Secondary Information:	
Corresponding Author's Institution:	Suzhou Institute of Nano-tech and Nano-bionics
Corresponding Author's Secondary Institution:	
First Author:	Guangyong Li
First Author Secondary Information:	
Order of Authors:	Guangyong Li
	Guo Hong
	Dapeng Dong
	Wenhui Song
	Xuetong Zhang
Order of Authors Secondary Information:	
Abstract:	Wearable devices and systems demand multifunctional units with intelligent and integrative functions. Smart fibres with response to external stimuli, such as electrical, thermal and photonic signals etc., as well as offering energy storage/conversion, are essential units for wearable electronics, but still remains great challenges. Herein the flexible, strong and self-cleaning graphene aerogel composite fibres, with tunable functions of thermal conversion and storage under multi-stimuli, have been fabricated. The fibres made from porous graphene aerogel/organic phase change materials coated with hydrophobic fluorocarbon resin, rendered a wide range of phase transition temperature and enthalpy (0-186 J/g). The strong and compliant fibres were twisted into yarn and woven into fabrics, showing a self-clean super-hydrophobic surface and excellent multiple responsive properties to external stimuli (electron/photon/thermal) together with reversible energy storage and conversion. Such aerogel-directed smart fibres promise for broad applications in the next-generation of wearable systems.

DOI: 10.1002/((please add manuscript number))
Article type: Communication

Multi-responsive Graphene Aerogel-directed Phase Change Smart Fibres

*Guangyong Li, Guo Hong, Dapeng Dong, Wenhui Song, Xuetong Zhang**

G. Li
School of Materials Science and Engineering, Beijing Institute of Technology, Beijing, 100081, P. R. China.
G. Li, D. Dong, Prof. X. Zhang
Suzhou Institute of Nano-Tech and Nano-Bionics, Chinese Academy of Sciences, Suzhou 215123, P.R. China.
E-mail: xtzhang2013@sinano.ac.cn
Prof. G. Hong
Institute of Applied Physics and Materials Engineering, University of Macau, Macao.
Prof. W. Song
Centre for Nanotechnology and Regenerative Medicine, Division of Surgery and Interventional Science, University College London NW3 2PF, United Kingdom

Keywords: graphene aerogel, smart fibre, phase change materials, electrical/thermal/optical stimuli

Abstract: Wearable devices and systems demand multifunctional units with intelligent and integrative functions. Smart fibres with response to external stimuli, such as electrical, thermal and photonic signals etc., as well as offering energy storage/conversion, are essential units for wearable electronics, but still remain great challenges. Herein the flexible, strong and self-cleaning graphene aerogel composite fibres, with tunable functions of thermal conversion and storage under multi-stimuli, have been fabricated. The fibres made from porous graphene aerogel/organic phase change materials coated with hydrophobic fluorocarbon resin, rendered a wide range of phase transition temperature and enthalpy (0-186 J/g). The strong and compliant fibres were twisted into yarn and woven into fabrics, showing a self-clean super-

hydrophobic surface and excellent multiple responsive properties to external stimuli (electron/photon/thermal) together with reversible energy storage and conversion. Such aerogel-directed smart fibres promise for broad applications in the next-generation of wearable systems.

Smart fibres, a fundamental unit of textiles capable of responding to various external stimuli, have become an emerging driving force for advanced flexible and wearable systems, such as sensors, actuators, bionic implants, robotics, energy harvesting devices, thermo-regulating garments and heaters.[1] However current textile fibres, made from both natural or semisynthetic polymers, are intrinsically electrically and thermally insulating, which limits the choice of sensors and actuators made from the conventional electronic hardware and constrains the development of future wearable electronics and robotics. The development of nanocomposite fibres and nanofibres are currently of great interest. As reported in recent years, carbon nanostructured fibres, such as carbon nanotubes yarns and graphene fibres, promise to be lighter, stronger, tougher and more electrical/thermal conducting in the near future.[2] Nevertheless, more functions in response to multi-stimuli from complex environment and human-machine-interface, such as heat, temperature, stress, light, humidity, pH etc., are still challenging. [2a,3]

Organic phase change materials (PCMs) and their composites have been intensively studied for the usage as heat storage and conversion from the surrounding environmental irradiation and waste heat generated during manufacturing processes or from use of products.[4] Conducting metal foam, carbon nanotubes sponges and graphene aerogel encapsulated PCM composites were demonstrated substantial improvement in thermal/electrical conductivity and heat conversion efficiency compared with pure PCM, promising for applications of bulk products in the forms of sheets and panels.[5] Some efforts were made to develop PCM encapsulated polymeric fibre (e.g. Thermocules™, Outlast) or nanofibres by utilizing both spinnability and good mechanical properties of polymers as matrix.[6] Core-shell fibre containing TiO_2-PVP polymer composites as the shell and PCM as the core made by co-axial electrospinning was reported to respond and buffer the environmental temperature variation by absorbing/releasing thermal energy to provide a comfortable microclimate for either human body or housing precise instruments.[6a,7] However, such responses of the PCM-polymer fibres are difficult to collect because of the low electrical/thermal conductivity of both PCMs and polymer matrices.[6]

Aerogel is an excellent ultra-light-weight material with a 3D interconnected porous network.[8] The extraordinary capillary force can be used to incorporate other components to obtain a novel system with multiple responsiveness and integration of more functions.[2a,9] Mesophase-derived graphene aerogel based PCM composites developed in house exhibited sensitive responses to external stimuli and efficient energy conversion/storage; which is attributed to the high electrical conductivity of graphene.[5d] However the rigidity and uniformity of graphene aerogel-PCM composites are still beyond the requirements for robust and flexible wearable systems. It is proposed that the introduction of aerogel into the fibre structure should allow for impregnation of functional materials in controlled and scalable approaches, to achieve the uniformity and alignment of the structure. This maximizes the physical and mechanical properties within the fibre's confinement, and facilitates the design and manufacturing of the multi-responsive fibres.

In this work, aerogel-directed smart fibres (ASFs) were fabricated by impregnating PCMs into graphene aerogel fibres (GAFs) and finished by a coating of fluorocarbon (FC) resin. The resulting smart fibres consisted of an aligned 3D graphene network within which the spacing between the graphene sheets was fulfilled by PCMs. These smart fibres exhibited tunable temperature and enthalpy of the phase transition. Both the fibres and the fabrics demonstrated super-hydrophobic surfaces and excellent multiple responsive properties to external stimuli (electrical/thermal/photonic) with and without loading stresses, resulting in reversible heat conversion and storage. These tunable and multi-responsive smart fibres hold promise for applications in wearable fabrics and portable electrical devices suitable for a range of varying conditions.

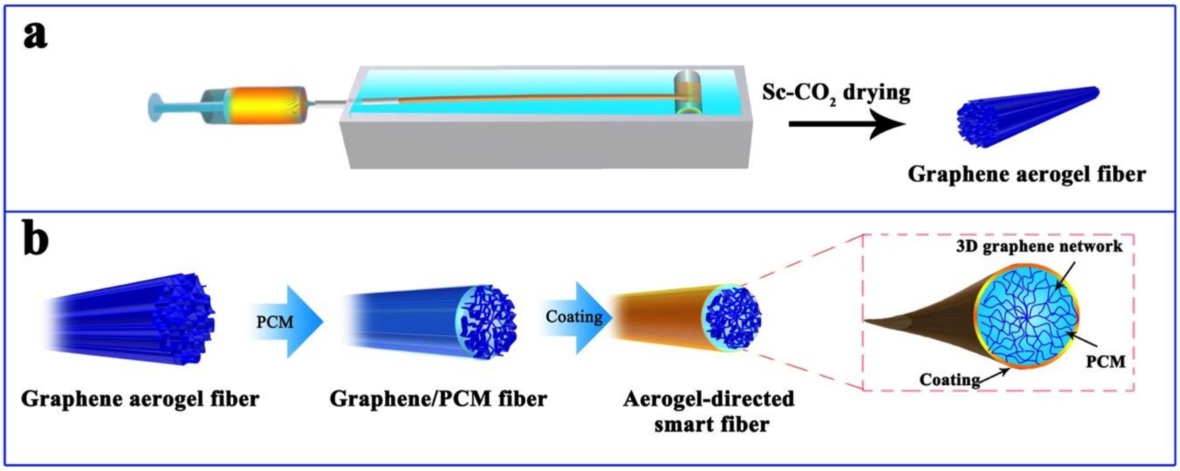

Scheme 1. Schematic description of the processes of graphene aerogel fibre (a) and graphene/PCM smart fibres (b).

The synthetic pathway of graphene/PCM ASF is shown in **Scheme 1**. It involves the synthesis and spinning of GAF, impregnation of PCMs and then an outer coating of the hydrophobic resin. GAF was first prepared by injecting and spinning a uniform GO liquid crystal into Vitamin C (VC)/HCl solution with subsequent reduction and supercritical fluid drying in sequence (Scheme 1a). The GAF is comprised of a 3D interconnected porous network with a high specific surface area (548 m^2/g) and pore volume (2.27 cm^3/g), (Figure S1-2 in Supporting Information), generating the extraordinary capillary action throughout the fibre to absorb PCM resins (such as paraffin and PEG) easily. The fibre was finished by coating a protective layer of fluorocarbon resin (Scheme 1b). An optimized smart fibre consists of 83 wt% polyethylene glycol (PEG4000), a PCM impregnated continuous graphene aerogel network and a super-hydrophobic coating. The high loading PEG with a relatively high molecular weight is envisaged to contribute to the high phase change enthalpy and well-balanced mechanical properties of the ASF fibre among other PCM based fibres, as showed in **Figures 1-2** and Tables S1-S2.

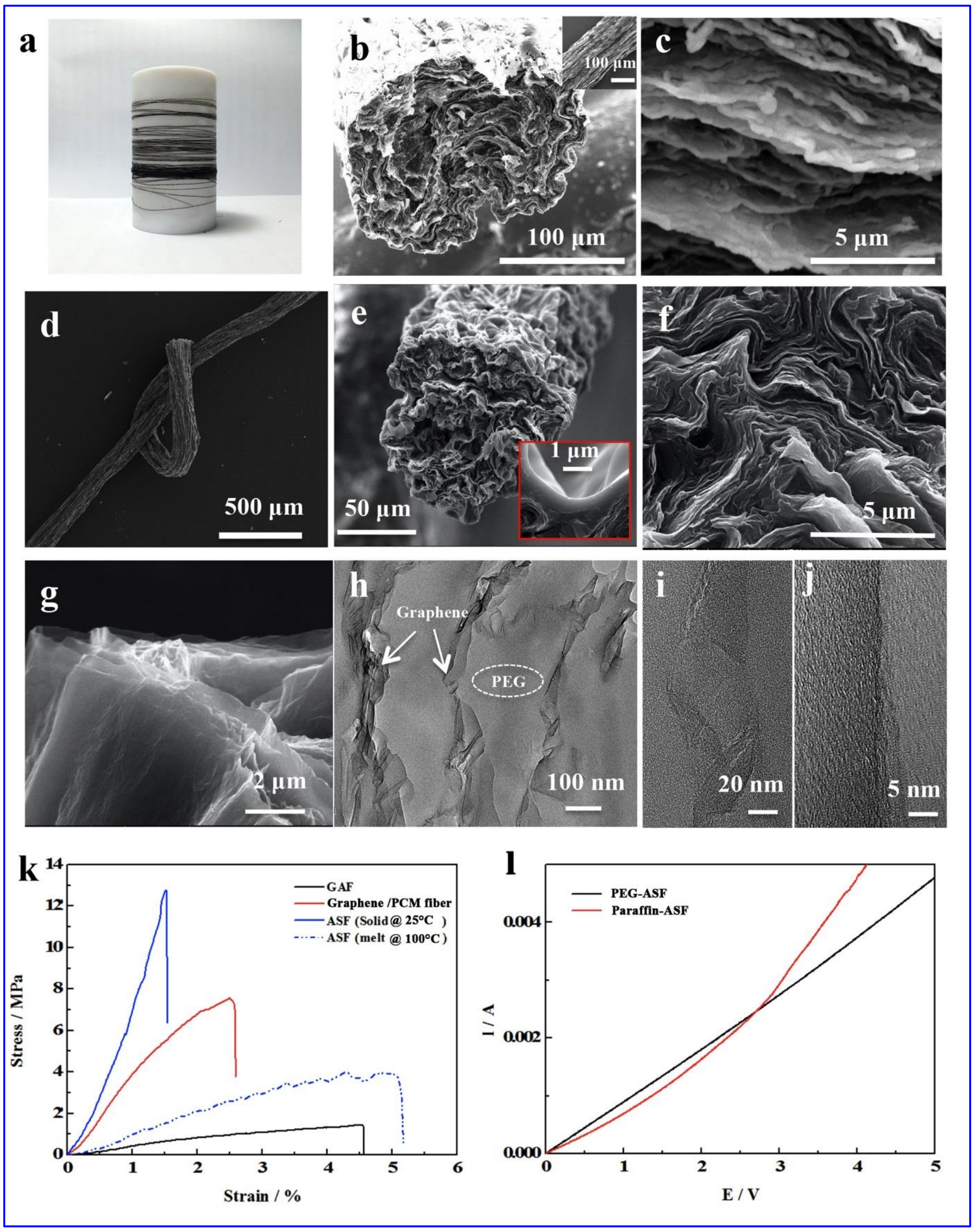

Figure 1. (a) The aerogel-directed smart fibre, ASF, as spun. (b-c) SEM images showing the morphology of cross section of paraffin-based ASF. (d-g) SEM images showing the knot and cross section of PEG based ASF. (h-j) TEM images showing few layers of graphene coated by PEG in a PEG based ASF. (k) Tensile stress-strain curves of PEG-ASFs at 100 °C and 25 °C), graphene/PEG4000 composite fibre and GAF. (l) *I-E* curves of ASFs.

The field emission scanning electron microscopy (FESEM) and transmission electron microscopy (TEM) were applied to reveal the hierarchical structure of the PEG-ASF. As shown in Figure 1b-f and Figures S1 and S3, SEM images of ASF cross-sections showed that the graphene sheets were stacked and wrapped in parallel, aligned with the fibre's long axis and the pores were fully filled by PEG and few bare graphene sheets were observed in cross section of ASF, indicating a strong adhension between graphene and PEG. When examined at a relatively high resolution (Figure 1c, 1g), uniform nano-laminate structures between the graphene sheets and PCM resin were observed. There is a smooth and dense skin layer formed by the fluorocarbon coating around the fibre (inset of Figure 1e and Figure S4 in Supporting Information), which gives the fibre surface superhydrophobic property. Furthermore, TEM images were taken from the cross section reveal the interface of the nano-laminate at nanoscale. The ribbon-like graphene sheets in Figure 1h are evenly covered by a PEG layer though still visible at the edge of PEG/graphene walls, and high-resolution TEM images (Figure1i-j) shows that the nano-laminate consists of graphene sheets in a few layers and even a single layer stacking between PEG.[10] Furthermore, the presence of PEG and FC coating on the surface of the ASFs was confirmed by XPS spectra (Figure S5-6, Supporting Information).

The resulting smart fibres consisting of the continuous PEG/graphene nano-laminates throughout the aerogel network and the super-hydrophobic coating, exhibited excellent strength and elasticity: it can be either tied into a knot (Figure 1d), entwined with commercial Outlast fibre (**Figure 2d** and Figure S7) or woven into fabrics (Figure 2e and g). Mechanical measurements demonstrated that ASFs exhibited typical stress and strain profiles at room temperature, similar to polymeric fibres under tensile loading (Figure 1k, Figure S8 and Table S1). The fracture strength (12.7 MPa) of PEG-ASF is 70% higher than graphene/PEG fibre (7.5 MPa) and 775% higher than GAF (1.45 MPa), and the Young’s modulus of PEG-ASF (1.2 GPa) is 4 times higher than of graphene/PEG fibre (300 MPa) and 48 times higher than

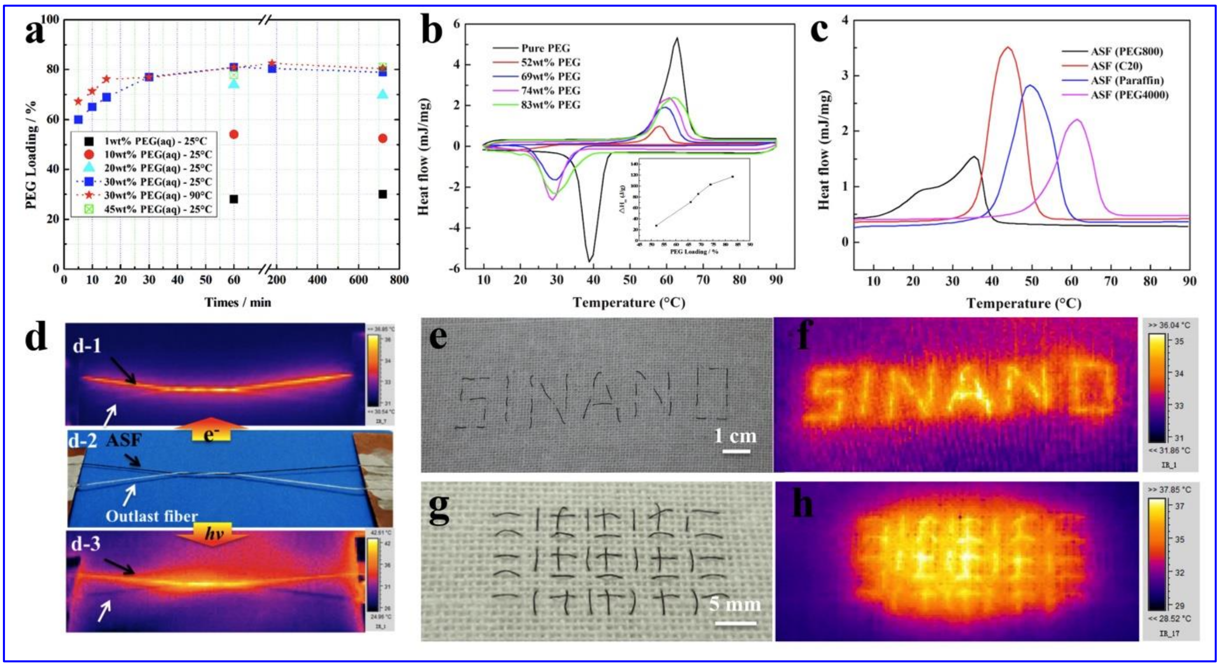

Figure 2. (a) The effect of impregnation temperature and time on the loading of PEG into GAF. (b) The DSC curves of ASFs and pure PEG, and the inset diagram shows the relationship between the latent heat and PEG loading content, (c) the melting DSC curves of ASFs impregnated with different PCMs: PEG800, PEG4000, C20 and Paraffin. (d) The infrared (IR) images of the twined PEG-ASF/Outlast fibre (d-2) under electric field (d-1) and light irradiation (d-3), respectively. The photograph (e) and IR image under light irradiation (f) of PEG-ASF in a letter pattern (SINANO) sewn on a white fabric. The photograph (g) and IR image under light irradiation (h) of ASF (black) woven together with cotton fabric (white).

GAF (25 MPa). Clearly PEG as a matrix and a large interface of the nano-laminates contributed most to the increase of both strength and stiffness of the fibre. The FC coating layer further enhanced both the strength and stiffness of the fibre but with a trade-off of a reduction of the fracture strain from 2.5% to 1.52%. The overall mechanical properties of ASF are attributed to the coherent core-shell structure of ASF: the compact stacking of graphene sheets/PEG nano-laminates and the FC coating.[10] At the melting state of PEG (100 °C), the shape and dimension of ASF remained, while the fracture strength and Young's modulus of ASF reduced substantially compared to both ASF and composite fibre in solid (25 °C). However, the fracture strain, 5.06 %, increased nearly 3 times than in the solid stage (1.5%), and the fracture toughness increased nearly by 50%, from 82.5 to 122.4 kJ/m^3, still outperforming pure GAF. This confirms again the strong interaction between graphene sheets and PEG throughout the aerogel network regardless of the softening effect of PEG in its melted state.

The electric conductivity of ASFs were investigated by *I-E* curves, and the ASF exhibited excellent electric conductivity with ~370 S/m for PEG 83 wt% loading and ~1450 S/m for PEG 53 wt% loading (Figure S9), compared to the graphene aerogel fibre (~10^3 S/m)[10] and higher than the anisotropic graphene aerogel (341 S/m)[5d]. Interestingly, ASFs with different PCM matrices exhibited different electric behaviours. As shown in Figure 1l, the ASF with PEG exhibited a linear *I-E* curve, while ASF with paraffin showed a less linear one with a clear turning point. This might come from different states of phase change and polarization of paraffin,[11] which consists of a mixture of hydrocarbon molecules containing between twenty and forty carbon atoms at different voltages. We previously reported that graphene aerogel/paraffin nanocomposite generated high electro-heat at high voltage.[5d] Paraffin with short carbon chains tended to reach its phase transition earlier and polarised fast when increasing the voltage, compared to those with long carbon chains. The liquid part of paraffin could cause denser packing of graphene network of the fibre, plus more polarized paraffin at a high voltage, contributing to the nonlinear increase of the current. In contrast, the PEG used consists of uniform macromolecules with a molecular weight of M_n=4000, averaged from a narrow distribution (3600-4400). The resulting small and uniform crystalline structure of PEG within the graphene network may be related to more linear *I-E* relationship of the PEG-ASF.

As the fundamental paramenters for understanding, design and control of the thermal energy storage and release, the thermal properties of the ASFs were investigated. The phase transition of the ASFs with different loading contents of PCM was characterized by differential scanning calorimetry (DSC), as shown in Figure 2a-c. Through changing the impregnation conditions, i.e. the concentration of PEG4000 solution, temperature and time, the ASFs with various PEG loading from 0 to 84 wt.% were produced (Figure 2a, Figure S10-S12 and Table S2 in Supplementary Information). The DSC curves in Figure 2b show a downshift of the onset point and peak temperature of each the PEG-ASF to a lower temperature in a range of 48-53 °C and 56-59 °C, respectively, compared to pristine PEG with a melting onset point of 57.06 °C with a peak at 64.26 °C. The less PEG that was loaded, the lower the transition temperature shifted. This down-shift of the phase transition may be contributed by the confinement of the graphene network that reduced the PEG crystal size and crystallinity degree, and the large interface between PEG and graphene sheets that enhanced both thermal and electrical conductivity of the nanocomposite fibre (Figure 1l), and thus accelerated uniform heat dissipation within the PEG layer.[5b,d] The other types of PCM impregnated fibres showed a similar trend of phase change at different melting points (Figure 2c), such as PEG800 (about 24 °C), C20 (about 34 °C) and paraffin (about 42 °C).

The phase change enthalpy is also correlated to the loading of PEG in the ASF. From Figure 2b, the pristine PEG4000 had a melting enthalpy of 188.4 J/g. In the case of ASFs with 34 wt.% PEG, there was no endothermic peak scanned by DSC (Figure S10) and sharp Bragg peaks in X-ray diffraction spectrum (Figure S13) which indicated that the thin layer of PEG confined within the graphene sheets was in the presence of amorphous phase. When the PEG loading was increased to 52 wt.% and above, the phase transition of PEG emerged and its corresponding enthalpy increased almost linearly with the loading of PEG (inset of Figure 2b). When the PEG loading reached 83 wt.%, the enthalpy was measured as ~124 J/g, which is much higher than that of the commercially available Outlast air-conditioning fibre (~4 J/g, Figure S14) and other PCMs reported elsewhere.[6a,6c,6d,12] Even more intriguingly, the phase transition of the ASF occurred in all the 20 cyclic scans of heating and cooling at scanning rate 10 °C/min were virtually identical (Figure S15), indicating the excellent reversibility, efficiency and stability of heat conversion and storage of the fibre.[5d] The phase change enthalpy was also varied by introducing other PCMs (Figure 2c), such as paraffin (about 176 J/g) and *n*-eicosane (C20, about 186 J/g). Noteworthy, the ultra-thin layer of fluorocarbon coating did not interfere the phase transition of the fibres including the enthalpy, temperature of the phase transition and thermal stability (Figure S16-17).

The structure and properties of the nanocomposite based ASF revealed above render unique functions in response to different external stimuli (e.g. electrical or photonic) with simultaneous change of temperature. Figure 2d shows the IR images of a twined thread of ASF/Outlast fibres under an electric field (voltage 30 V) and light irradiation (1.0 sun, AM 1.5, 100 mW/cm^2, more details in Figure S18, Supporting Information.) respectively, indicating an increase of the temperature only along the ASF rather than the Outlast fibre (Figure 2d). From the measurement of the temperature vs the irridiation time, a near equilibrium temperature of the single ASF was reached at ~15s (Figure S19a-b). Similar responses were also demonstrated in 'SINANO' letter pattern and network woven fabrics of ASF/cotton under light irradiation (Figures 2f and h, Figures S19-S23). As expected, the ASF bundle and ASF/cotton fabrics demonstrated higher heating rate and higher temperature than single ASF, indicating faster heat trasfer, less heat loss within the ASF bundle and the fabrics. The comparison between Outlast fibre, single ASF, ASF bundle and ASF/cotton fabrics clearly indicate that the graphene network within the ASF fibres played essential multiple roles of electron transfer, photo captor and heat dissipation in inducing and facilitating the phase transition of PCM (PEG in this case) impregnated within the network (Figure S19-25 in Supporting Information).[5b,5d,13]

The responsive functions of ASF under different stresses and environmental conditions (temperature, moisture) were further investigated as shown in **Figure 3** and Figure S19-22. The temperature of the fibre in a bended “loop-like” shape (Figure 3a-a1) remained steady (about 40 °C) when the input voltage was 30 V, similar to the straight fibre at the same voltage as shown in Figure S24, further indicating the good adhesion between the PCM and graphene fibre (Figure S26). Furthermore, when the fibre was tied into a knot (Figure 3b-b1), the temperature increased to up to 72 °C, confirming the structural stability of fibre under 360° bending and twisting deformation.[14] It was notified that the elevated temperature distributed mostly along the straight line shortcut of the knot instead of the whole loop, indicating a lower interface contact resistance between the self-twined part of the knot compared to the resistance along the large circular part of the knot loop. This observation may be attributed to an increase of electrical and thermal conductivity of the fibre induced by the compressed and twisted graphene networks within the knots. It is also worth mentioning that the super-hydrophobic coating did not shade the electric conductivity, in fact, it may provide the electronic tunneling, to accelerate the electron transfer between the fibres owed to high electronegativity of fluorocarbon molecules (Figure S27). More pronounced electro-thermal responses of a fibre bundle at 30 V electric field support these speculations with the temperature reaching ~56 °C (Figure 3c-c1), and even higher to about 100 °C when the fibre bundle was tied into a knot (Figure 3d-d1).

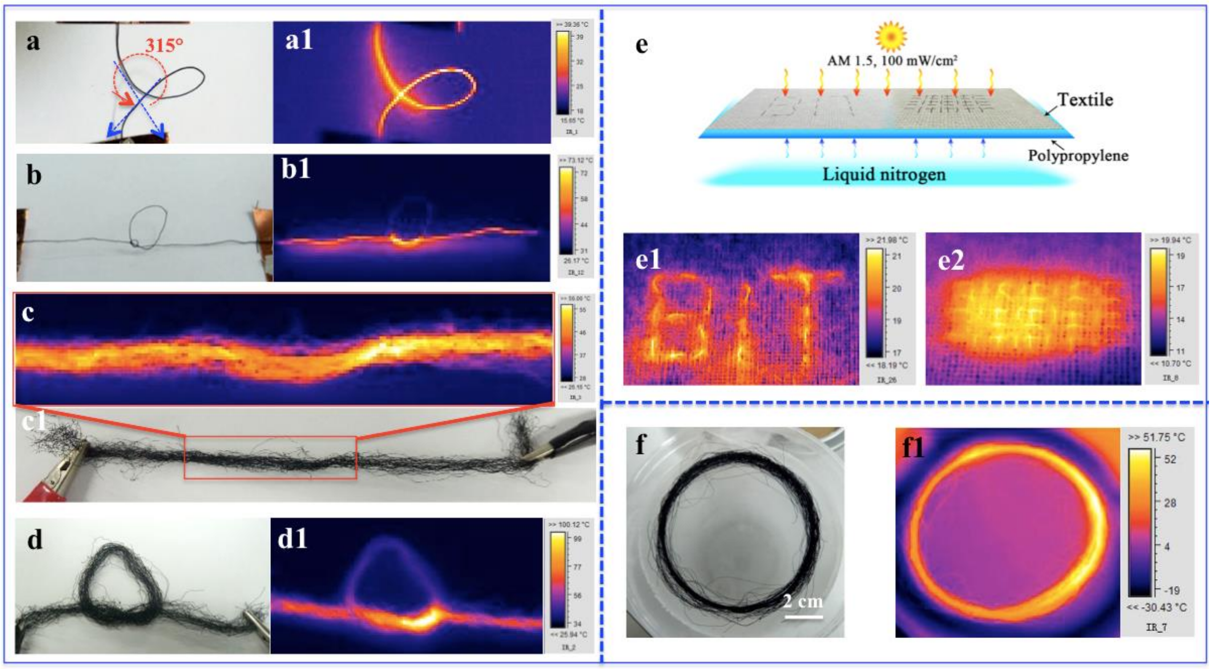

Figure 3. Photograph and IR images of the ASF by applying an input voltage about 30 V (a-d) and under solar irradiation (e-g). The single fibre, 5 cm long, was bent to a "loop-like" shape with a bending angle of 315° (no contacted site along this fibre) a-a1) and tied into a knot (about 5 cm length, b-b1) under 30 V electric field. The fibre bundle before (30 cm length, c-c1) and after (d-d1) tied into a knot under 30 V electric field. (e-f) Schematic and IR images of the photonic response of ASF textile in a cold environment (selecting a temperature of ~ 0 °C). Single ASF/cotton woven fabric (e1-e2) and a fibre bundle (f-f1) placed on a cold polypropylene (PP) surface under solar illumination of 1.0 sun.

As a black body, the ASF can also respond to irradiation from the surrounding environment and generate heat simultaneously.[5d] Under simulated solar illumination with an intensity of 1.0 sun, the photo-to-heat response in the low temperature environment (~ 0 °C) were investigated (Figure 3e-f1). A single ASF woven into a "BIT" letter pattern (Figure 3e1) and network fabric (Figure 3e2) could generate a warm surface at a human comfortable temperature around 19-21°C under solar irradiation, in contrast to the freezing temperature of the surroundings, indicating an highly efficient photo-heat conversion and storage occurred along the single fibre regardless of a cold environment. Furthermore, the temperature of a bundle of the ASF fibres placed directly on the cold surface could reach even higher, 45-50 °C (Figure 3f-f1), more than double compared to the single ASF/cotton fabrics under the same solar irradiation. The temperature-time curves of single ASF and ASF/cotton fabrics were also recorded (Figure S19-S22 and S28, Supporting Information). The fast heating and thermal storage/release (temprature plateau) of the fabrics were demonsrated with an estimated thermal energy conversion and storage efficiency of ASF/cotton Fabric 2, 61.5±1.6%. The fast heat transfer between the ASF fibres is envisaged to contribute to such pronounced and synergistic photo-thermal response from all the fibres in the bundle/fabrics (Figure S19 and S28).[15]

To investigate the super-hydrophobic surface property of the ASF, static water contact angle measurements were performed at room temperature. As shown in **Figure 4a-c** and Figure S29, the water droplets retained a nearly spherical shape on the surface of a single ASF with an approximate static contact angle of about 158 °, confirming the super-hydrophobic nature of the fibre surface, while the GAF, graphene/PEG composite fibre and pure PEG were hydrophobic (124 °), hydrophilic (<60 °), and super-hydrophilic (9.4 °) respectively. Such a non-wetting property allowed the fibre to be removed easily from the water droplet, which was suspended by a metallic needle, leaving no visible traces of water on the fibre's surface and without the water droplet falling, as shown in Figure 4d. Even though the water droplet was slightly stretched by the fibre just before its departure, the shape of droplet retained, indicating weaker adhesion between the fibre and the water droplet as compared to that between the needle and the droplet.[16] As expected, the ASF bundle also exhibited the super-hydrophobic property, with water droplets dyed in different colours maintained perfectly spherical on the bundle fibres' surfaces (Figure 4e-e1).

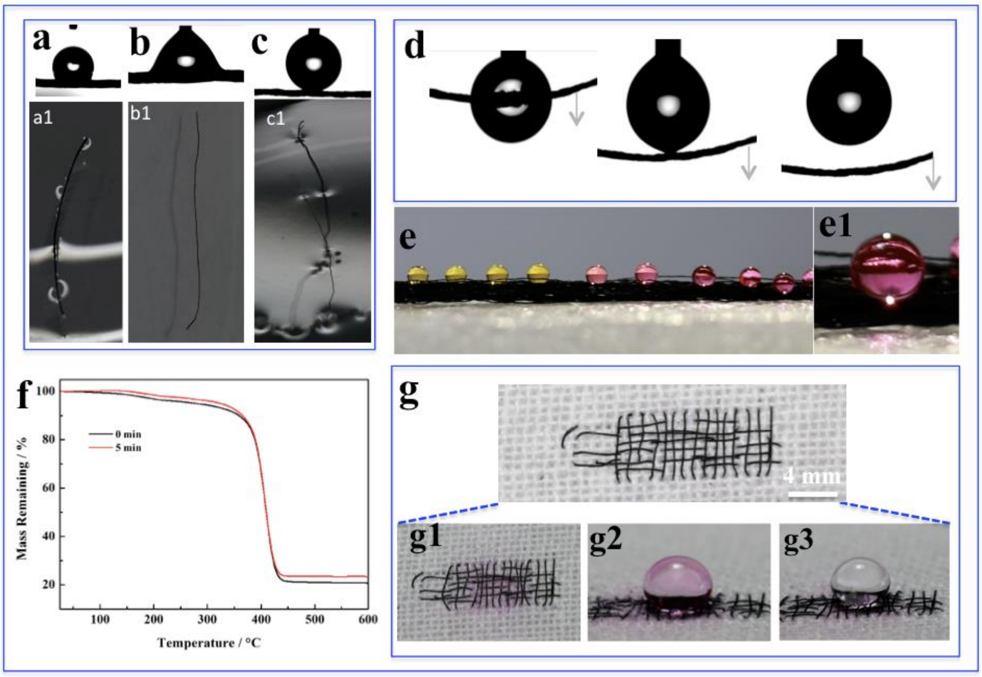

Figure 4. Photographs of the contact angle measurement and graphene aerogel fibre (a-a1), graphene/PEG composite fibre (b-b1) and ASF (c-c1) on the surface of water, pulling out ASF fibre from the water droplet (d). Superhydrophobic surface property of the ASF fibre bundle (e-e1). TGA curves ofASF fibre before and after being soaked in water for 5 minutes. (f). The self-cleaning function of ASF woven fabric (g1-g3).

The super-hydrophobic property renders ASF the ability of waterproof and self-cleaning. After the ASF was immersed in water for five minutes, TGA weight loss profile shows no trace of water absorption into the fibres and reduction of thermal stability of the fibre, despite the hydrophilic nature of PEG in this case (Figure 4f), mainly owing to FC coating on the surface and two ends of the fibres (Figure S5-S6 and S30-31). In contrast, the loading content of PEG in GAF without FC coating decreased from ~74 wt% to 66 wt%, with nearly 10 % weight loss after soaking (Figure S32). The self-cleaning function was demonstrated on the surface of the ASF woven fabric contaminated by white powders containing Rhodamine B (RhB) dye (Figure 4g-g3, and Movie S1): a colourless water droplet became magenta immediately when it contacted the powder on the fibre surface. Subsequently, the magenta water droplet could move around, taking and dissolving the rest of the powder on the super-hydrophobic surface of the fibre without changing its shape. Another experiment further demonstrated self-cleaning function of the ASF. When RhB dye solution was dripped on a random ASF coil, the large water droplets could not stay on the mesh, instead they went through the fibre mesh and were absorbed by white paper underneath (Figure S33). As a result the white paper was dyed magenta while the fibre was not wetted (Figure S33). Even when the fibre mesh was immersed into magenta water, it still maintained clean without residue dye on the fibres (Figure S34-36). The self-celaning function of the ASF fibre described above, reiterates the superhybrophic nature of the FC coated fibres. The high contact angle of the ASFs offers low surface energy and weak interfacial tension that prevents water and RhB dye particles from adhering to or diffusing into the fibres.

In brief, a variety of multi-responsive smart fibres with a wide range of tunable phase transition temperatures and enthalpy have been produced through impregnation of different types of organic PCMs into graphene aerogel fibre. The strong capillary action in the highly porous graphene aerogel network generated uniform nano-laminates between graphene sheets and PCM along the micro-fibre, resulting in overall superior mechanical, electrical and thermal properties. A diverse range of smart fibres with adjustable phase transition temperatures and phase change enthalpies have been developed though the selection of different types of PCMs and controlling PCM loading (up to 84% wt%) during the impregnation process with the latent heat reaching up to 124 J/g for PEG-ASF, 176 J/g for wax-ASF and 186 J/g for C20-ASF. The unique nanostructure and superior properties of PCM nanocomposite fibres have been demonstrated through electro-thermal and photo-thermal functions in response to multi-stimuli (electron/photon) and environmental irradiation with high efficiency, stability and reversibility. A super-hydrophobic fluorocarbon coating has added a self-cleaning feature and further enhanced the mechanical properties of the fibres. The robustness and compliance of the knot and woven fabric made from these aerogel-directed smart fibres, plus the appealing multi-responsive functions, including energy conversion and storage, is promising for a range of novel smart units for future flexible and wearable devices, e.g. smart wearable fabrics (Figure S25) and clothes suitable for climbing in frigid zones.

Experimental Section

Materials: Graphite powder (1μm) was purchased from Qingdao Tianheda Graphite Co., Ltd, Qingdao, China. P_2O_5, $K_2S_2O_7$, 30% H_2O_2, HCl (aq), and H_2SO_4 were obtained from Sinopharm. Chemical Reagent PEG, n-eicosane and L-AA were obtained from Aladdin Company. Paraffin (OP44E) was obtained from Ruhr Tech, Hangzhou, China. Fluonocarbon (FC) resin was obtained from Sino-Fluorine Science and technology Ltd, Shenzhen, China.

Preparation of GO-LC: Graphene oxide (GO) sheet was prepared from graphite powder by a modified Hummer method reported in our previous study, Liquid crystalline GO was obtained by centrifugation of the GO dispersion at high-speed (1700 rpm) for 4.5 h.[5d]

Preparation of graphene aerogel fiber (GAF): The resulting GO liquid crystal (~50 mg mL-1) was spinning into GO/VC (aq), allowed to stand for 12 h at 50 °C water bath. Followed by washing at least 4 times with absolute ethyl alcohol to replace the water, supercritical drying with CO_2 (40 °C, 10 MPa) for 12 h, the GAF was obtained.

Preparation of the aerogel-directed smart fiber (ASF): Both GAF and phase change materials (PEG or paraffin) were heated to 75-80 °C in a vacuum oven and were placed for 3 h for the GAF to be infused with PCM. After the GAF was submerged in the melting PCM, the system was allowed to hang under 80 °C, then the excess PCM adhered on the fiber surface will be removed. After cool down to room temperature, the composite fiber was obtained. Subsequently coating with fluorocarbon resin, the smart fiber can be obtained. The ASF with different loading PEG were prepared via similar method, difference was the PEG solution was used to replace the melt PEG.

Characterizations: The morphology of the samples was examined by SEM (Hitachi S-4800) with the acceleration voltage of 5-15 kV. The paraffin and the composite were coated with Au nano-powder under current of 20 mA for 2 min. Transmission Electron Microscope (TEM) measurement was carried out on Tecnai G2F20 S-Twin with the acceleration voltage of 200 kV; the TEM sample with about 40 nm thickness was prepared by cryo-cutting Raman spectra were recorded on a LabRAM HR Raman spectrometer with a 50mW He-Ne laser operating at 632 nm with a CCD detector. X-ray diffraction (XRD) patterns were recorded on a D8 Advanced spectrometer with a scanning rate of 0.05 s over an angular range of 5-65° (2θ). The pore size distribution and average pore diameter of the aerogels were analyzed by the BJH nitrogen adsorption and desorption method (ASAP 2020, Micromeritics, USA). The surface area of the aerogels was determined by the Brunauer-Emmett-Teller (BET) method, based on the amount of N_2 adsorbed at pressures $0.05< P/P0<0.3$. Thermal gravimetric analysis (TGA) and DTG was carried out using a TG 209F1 Libra (NETZSCH) analyzer with a heating rate of 10 °C min^{-1} in a nitrogen atmosphere. DSC analysis was performed on a DSC 200F3 NETZSCH with a heating and cooling rate of 10 °C min^{-1}. The electric resistances of the aerogel and its composites were measured by using a CHIChief 600D electrochemical workstation, and the electric conductivity can be calculated by the equation: $\kappa=IL/US$ where κ is the electric conductivity, I is the current which cross the sample, U is the voltage applied in the sample, L is the length of sample current goes through, S is the cross area of current. The stress-strain curves were measured by an Instron 3365 tensile testing machine. The contact angle was measured by OCA 15EC DATAPHYSICS INSTRUMENTS GMBH. Infrared photos were taken with a MinIR (M1100150) camera. The XPS spectra were measured by Escalab 250Xi, Thermo Scientific. The temperature-time curves were measured and recored by thermal couple and Keysight 34970 Data Acquisition.

Supporting Information

Supporting Information is available from the Wiley Online Library or from the author.

Acknowledgements

This work was financially supported by the National Key Research and Development Program of China (2016YFA0203301), the National Natural Science Foundation of China (51572285), the Natural Science Foundation of Jiangsu Province (BK20170428) and the Royal Society Newton Advanced Fellowship (NA170184). Wenhui Song would like to thank for the finance supports by the UK Engineering and Physical Sciences Research Council (EPSRC EP/L020904/1 and EP/M026884/1). Guo Hong would like to thank for the Start-up Research Grant (SRG2016-00092-IAPME), University of Macau and Science and Technology Development Fund (081/2017A2), Macao S.A.R (FDCT).

Received: ((will be filled in by the editorial staff))
Revised: ((will be filled in by the editorial staff))
Published online: ((will be filled in by the editorial staff))

References

[1] a) W. Zeng, L. Shu, Q. Li, S. Chen, F. Wang, X. M. Tao, *Adv. Mater.* **2014**, *26*, 5310; b) S. Pan, J. Ren, X. Fang, H. Peng, *Adv. Energy Mater.* **2016**, *6*, 1501867; c) K. Guo, N. Yu, Z. Hou, L. Hu, Y. Ma, H. Li, T. Zhai, *J. Mater. Chem. A* **2016**, *5,* 16; d) K. Jost, G. Dion, Y. Gogotsi, *J. Mater. Chem. A* **2014**, *2*, 10776.

[2] a) Z. Li, Z. Liu, H. Sun, C. Gao, *Chem. Rev.* **2015**, *115*, 7046; b) Y. Liu, Z. Xu, W. Gao, Z. Cheng, C. Gao, *Adv. Mater.* **2017,** *29*, 1606794; c) G. Xin, T. Yao, H. Sun, S. M. Scott, D. Shao, G. Wang, J. Lian, *Science* **2015**, *349*, 1083; d) W. Lu, M. Zu, J. H. Byun, B. S. Kim, T. W. Chou, *Adv. Mater.* **2012**, *24*, 1805; e) A. B. Dalton, S. Collins, E. Muñoz, J. M. Razal, V. H. Ebron, J. P. Ferraris, J. N. Coleman, B. G. Kim, R. H. Baughman, *Nature* **2003**, *423*, 703; f) K. Koziol, J. Vilatela, A. Moisala, M. Motta, P. Cunniff, M. Sennett, A. Windle, *Science* **2007**, *318*, 1892; g) J. Cao, Y. Zhang, C. Men, Y. Sun, Z. Wang, X. Zhang, Q. Li, *ACS Nano* **2014**, *8*, 4325; h) J. Li, J. Y. Li, L. F. Li, M. Yu, H. J. Ma, B. W. Zhang, *J. Mater. Chem. A* **2014**. *2*. 6359-6362.

[3] a) F. Zhao, Y. Zhao, H. Cheng, L. Qu, *Angew. Chem. Int. Ed.* **2015**, *54*, 14951; b) J. Lee, H. Kwon, J. Seo, S. Shin, J. H. Koo, C. Pang, S. Son, J. H. Kim, Y. H. Jang, D. E. Kim, *Adv. Mater.* **2015**, *27*, 2433; c) Q. Wang, M. Jian, C. Wang, Y. Zhang, *Adv. Funct. Mater.* **2017**, *27*, 1605657.

[4] a) D. Zhou, C. Y. Zhao, Y. Tian, *Appl. Energy* **2012**, *92*, 593; b) A. Sharma, V. V. Tyagi, C. R. Chen, D. Buddhi, *Renew. Sust. Energy Rev.* **2009**, *13*, 318.

[5] a) X. Xiao, P. Zhang, M. Li, *Appl. Energy* **2013**, *112*, 1357; b) L. Chen, R. Zou, W. Xia, Z. Liu, Y. Shang, J. Zhu, Y. Wang, J. Lin, D. Xia, A. Cao, *ACS Nano* **2012**, *6*, 10884; c) Z. Liu, R. Zou, Z. Lin, X. Gui, R. Chen, J. Lin, Y. Shang, A. Cao, *Nano Lett.* **2013**, *13*, 4028; d) G. Li, X. Zhang, J. Wang, J. Fang, *J. Mater. Chem. A* **2016**, *4*, 17042; e) X. Wang, G. Li, G. Hong, Q. Guo, X. Zhang, *ACS Appl. Mater. Interfaces* **2017**, *9*, 41323.

[6] a) J. McCann, A. Manuel Marquez, Y. Xia, *Nano Lett.* **2006**, *6*, 2868; b) C. Chen, L. Wang, Y. Huang, *Appl. Energy* **2011**, *88*, 3133; c) K. Iqbal, D. Sun, *Renew. Energy* **2014**, *71*, 473; d) G. Q. Wen, R. Xie, W. G. Liang, X. H. He, W. Wang, X. J. Ju, L. Y. Chu, *Appl. Therm.

Eng. **2015**, *87*, 471; e) E. Zdraveva, J. Fang, B. Mijovic, T. Lin, *Ind. Eng. Chem. Res.* **2015**, *54*, 8706.

[7] S. X. Wang, Y. Li, J. Y. Hu, H. Tokura, Q. W. Song, *Polym. Test.* **2006**, *25*, 580.

[8] a) A. C. Pierre, G. M. Pajonk, *Chem. Rev.* **2002**, *102*, 4243. b) J. H. Li, J. Y. Li, H. Meng, S. Y. Xie, B. W. Zhang, L. F. Li, H. J. Ma, J. Y. Zhang, M. Yu, *J. Mater. Chem. A* **2014**, *2*, 2934-2941.

[9] C. Liu, F. Li, L.-P. Ma, H.-M. Cheng, *Adv. Mater.* **2010**, *22*, E28.

[10] Z. Xu, Y. Zhang, P. G. Li, C. Gao, *ACS Nano* **2012**, *6*, 7103.

[11] a) M. Rákoš, *Czech. J. Phys. B* **1971**, *21*, 106; b) Y. Wang, H. Mi, Q. Zheng, Z. Ma, S. Gong, *ACS Appl. Mater. Interfaces* **2015**, *7*, 2641; c) K. Zhang，B. Han，Y. Xun, *Energy Convers. Manage.* **2012**, *64*, 62; d) C. Rajagopal, M. Satyam, *J. Appl. Phys.* **1978**, *49*, 5536.

[12] S. X. Sun, R. Xie, X. X. Wang, G. Q. Wen, Z. Liu, W. Wang, X. J. Ju, L. Y. Chu, *J. Mater. Sci.* **2015**, *50*, 5729.

[13] Y. Wang, B. Tang, S. Zhang, *Adv. Funct. Mater.* **2013**, *23*, 4354.

[14] R. Wang, Z. Xu, J. Zhuang, Z. Liu, L. Peng, Z. Li, Y. Liu, W. Gao, C. Gao, *Adv. Electron. Mater.* **2017**, *3*, 1600425.

[15] X. Zhao, W. Yao, W. Gao, H. Chen, C. Gao, *Adv. Mater.* **2017**, *29*, 1701482.

[16] M. Maleki, M. Shokouhimehr, H. Karimian, A. Beitollahi, *Rsc Adv.* **2016**, *6*, 51426.

TOC

A variety of multi-responsive smart fibres with a wide range of tunable phase transition temperatures and enthalpy have been produced through impregnation of different types of organic PCMs into graphene aerogel fibre and finished by coating flurocarbon resin layer, showing a self-clean super-hydrophobic surface and excellent multiple responsive properties to external stimuli (electron/photon/thermal) together with reversible energy storage and conversion.

Keyword: graphene aerogel, smart fibre, phase change materials, electrical/thermal/optical stimuli

*Guangyong Li, Guo Hong, Dapeng Dong, Wenhui Song, Xuetong Zhang**

Multi-responsive Graphene Aerogel-directed Phase Change Smart Fibres

ToC figure ((Please choose one size: 55 mm broad × 50 mm high **or** 110 mm broad × 20 mm high. Please do not use any other dimensions))

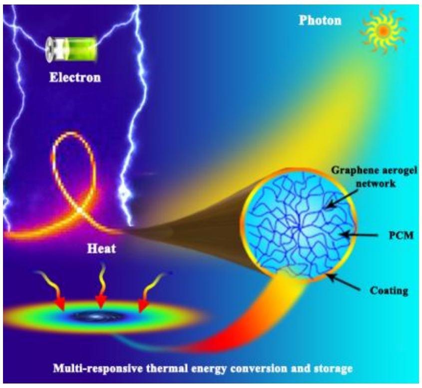

Supporting Information

Multi-responsive Graphene Aerogel-directed Phase Change Smart Fibres

*Guangyong Li, Guo Hong, Dapeng Dong, Wenhui Song, Xuetong Zhang**

Figures:

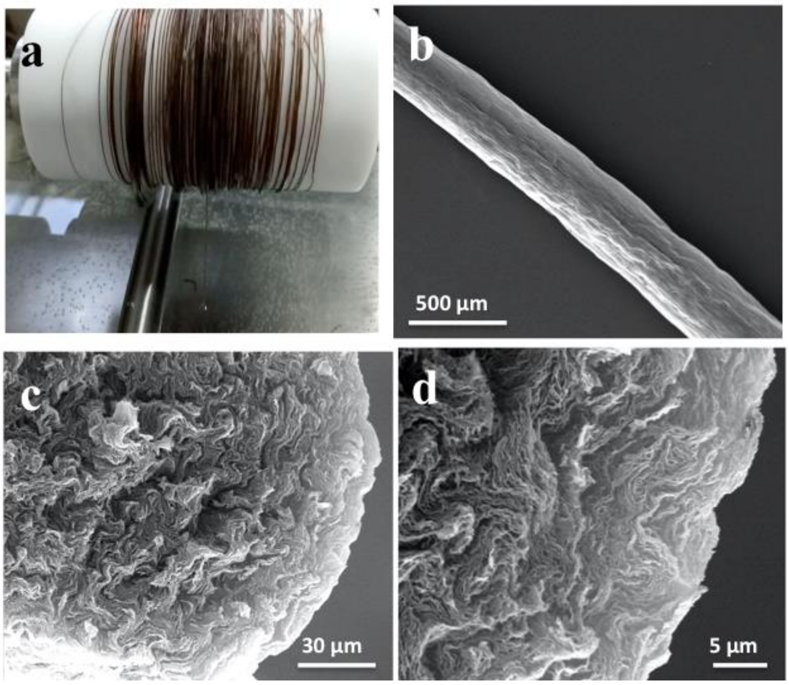

Figure S1 The photograph (a) of graphene oxide hydrogel fiber during spinning process. The SEM images (b-d) of graphene aerogel fiber (GAF), GAF was synthesized by spinning the uniform GO liquid crystal into VC/HCl solution and subsequent reduction and supercritical drying.

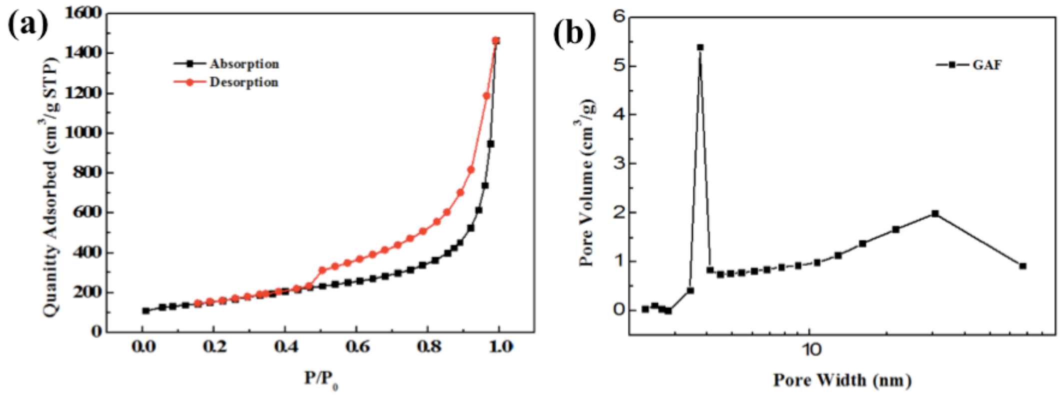

Figure S2 The N_2 adsorption and desorption isotherms (a) and pore size distribution of GAF (b).

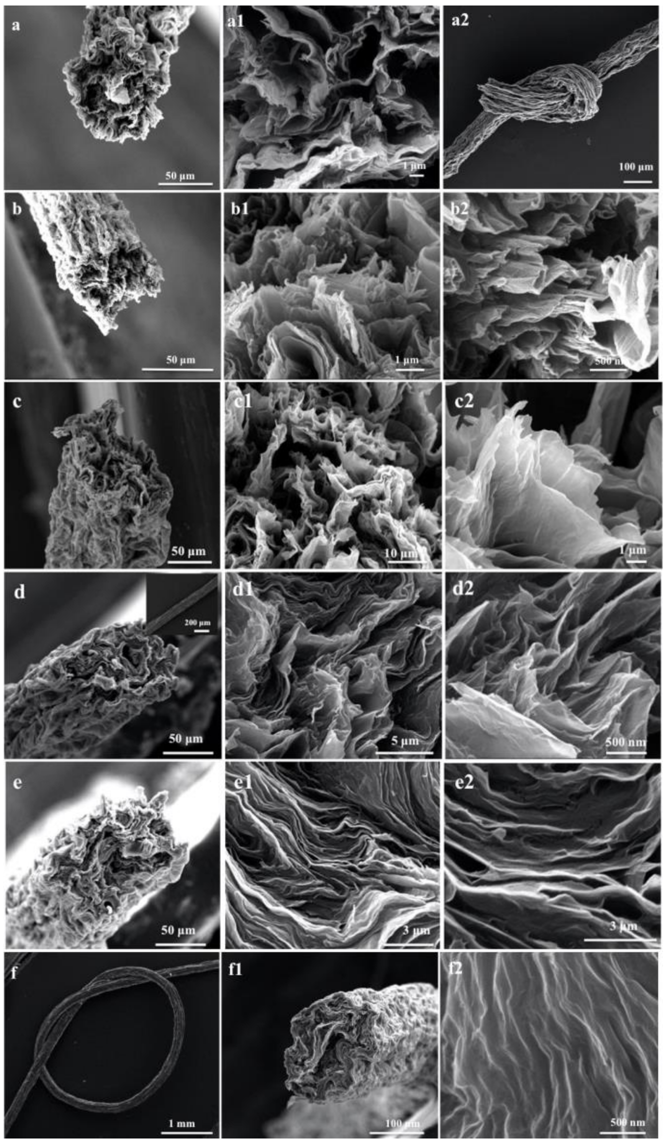

Figure S3 SEM images of cross section of composite fiber with different PEG loading, 0 (a), 30% (b), 52% (c), 69% (d), 75% (e), 81% (f).

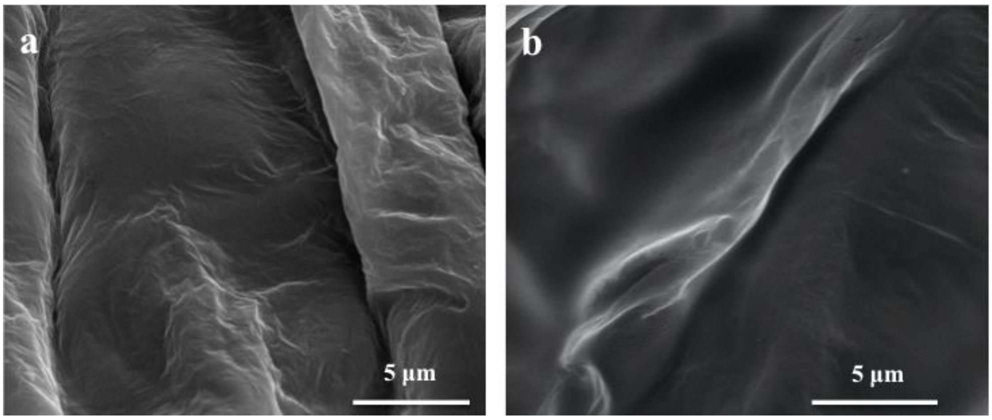

Figure S4 SEM images of the surfaces of fiber without (a) and with (b) coating.

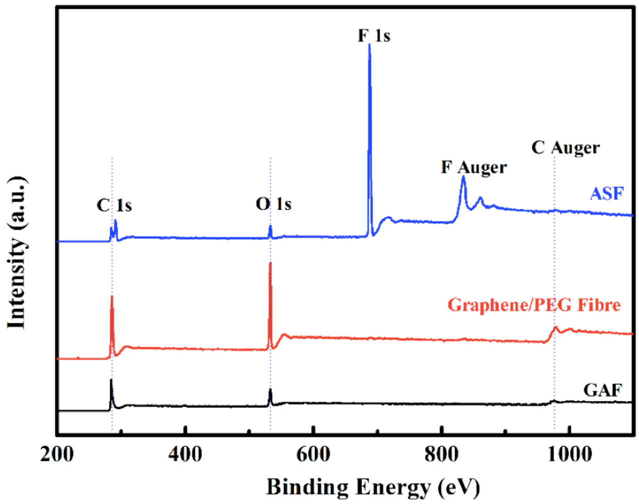

Figure S5 XPS survey spectra of GAF, graphene/PEG fibre and ASF. The ASF exhibits C1s, O1s, F1s peak at 284.4 eV, 532 eV, 688 eV, the graphene aerogel fibre and the graphene/PEG fibre only exhibit C1s and O1s peak.

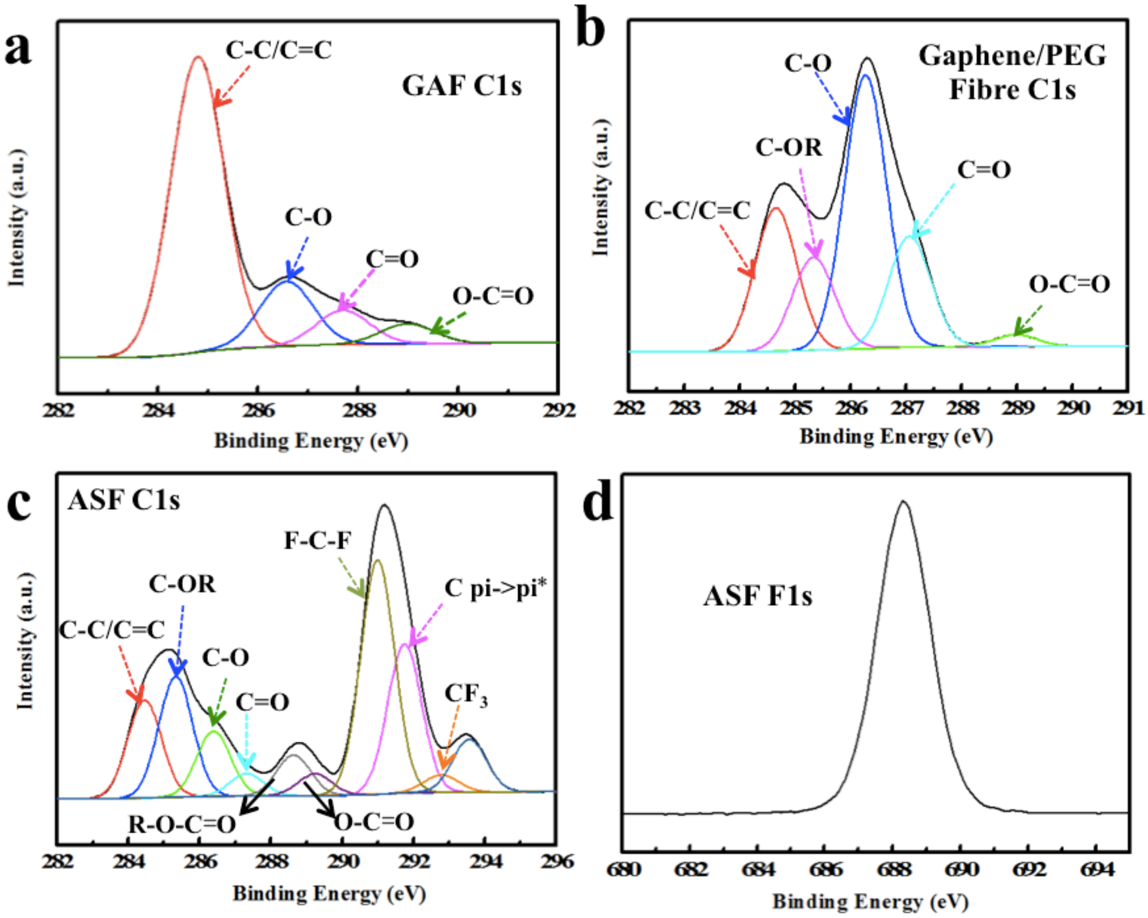

Figure S6 XPS C 1s spectra of GAF (a), graphene/PEG fibre (b) and ASF(c), and F 1s spectrum of ASF (d). Compared to graphene aerogel fibre, the graphene/PEG fibre exhibits C-O-R (PEG) peak at 285.3 eV, the ASF exhibited -CF_3 (293.5 eV), F-C-F peak (291.3 eV) and O=C-O-R peak (288.7 eV), and these chemical bonds derived from FC coating.

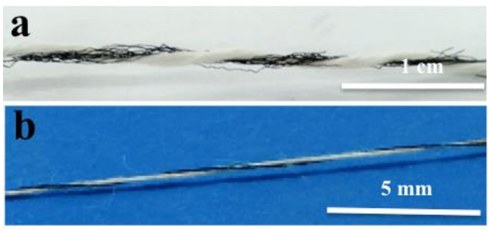

Figure S7 The twined ASF/outlast fiber structure.

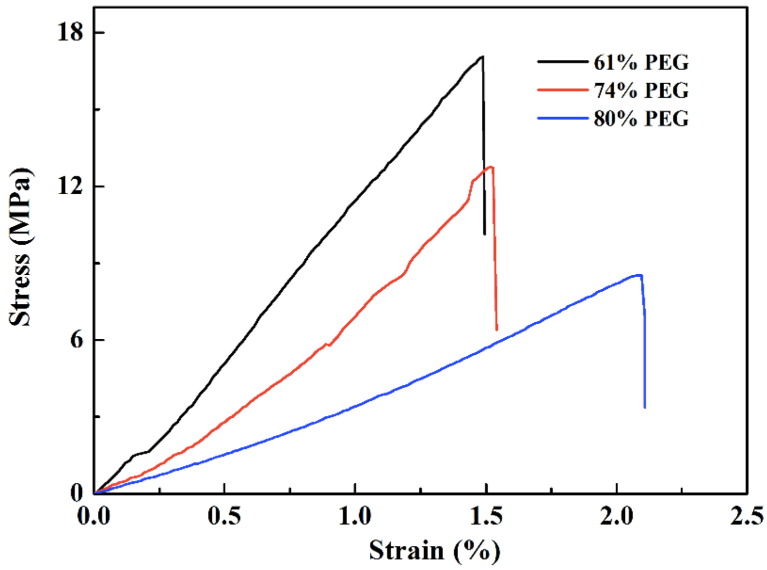

Figure S8 Mechanical measurements under tensile loading for ASFs with different PEG loading contents.

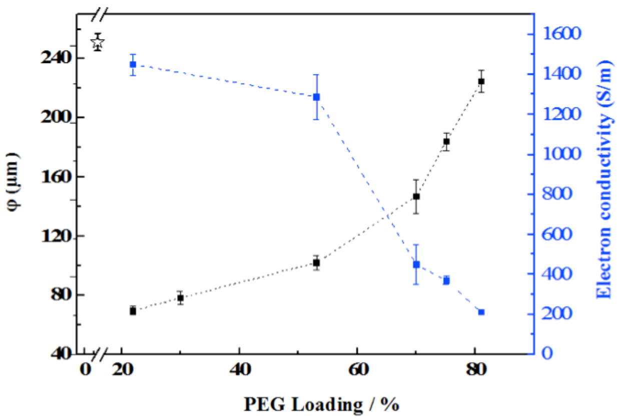

Figure S9 Diameters and electric conductivity of ASF with different PEG loading contents.

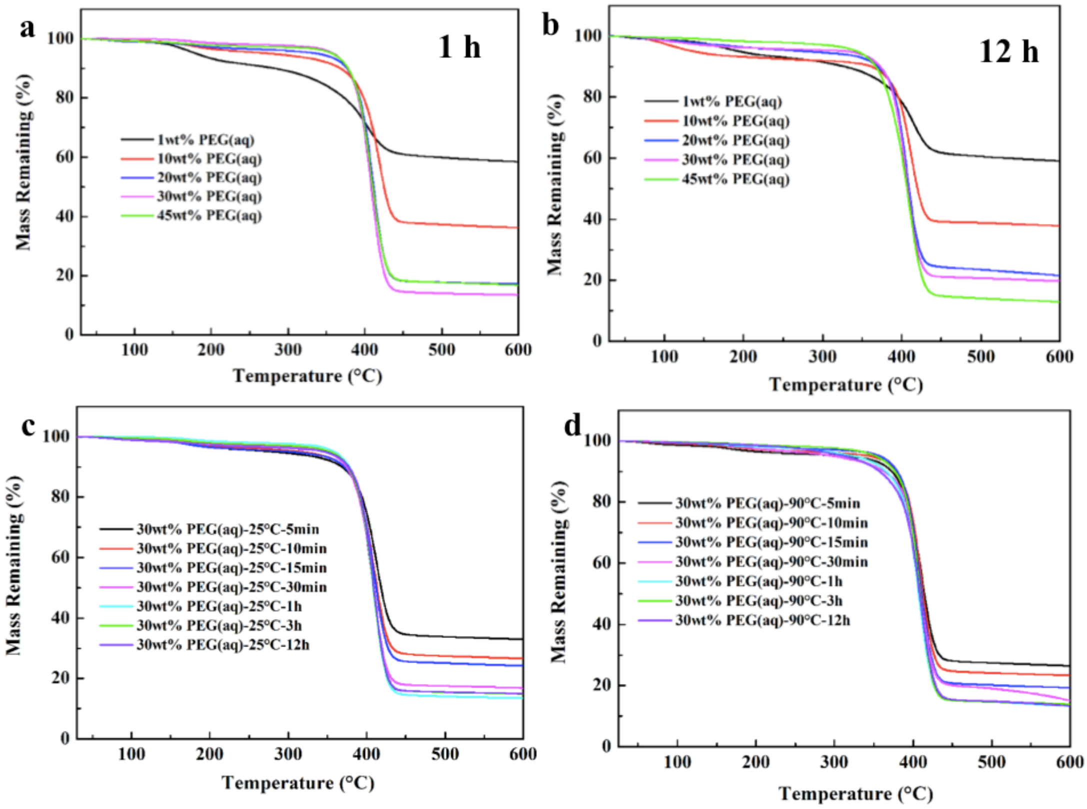

Figure S10 TG curves of composite fiber under different impregnation conditions.

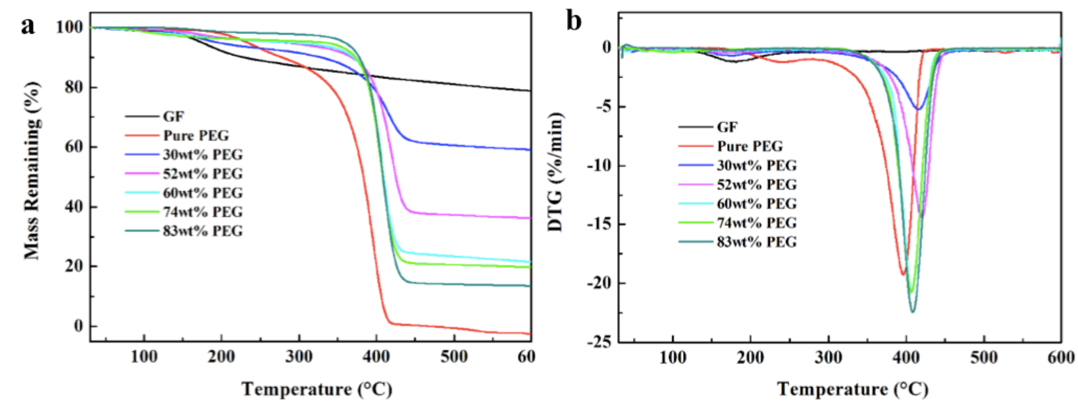

Figure S11 TGA (a) and DTG (b) curves of composite fiber with different PEG loading content, the thermal stability of PEG in fiber was better than pure PEG. The TGA results showed the combustion temperature of the aerogel-encapsulated PEG is higher than that of the pure PEG, suggesting strong interactions between PEG and graphene.

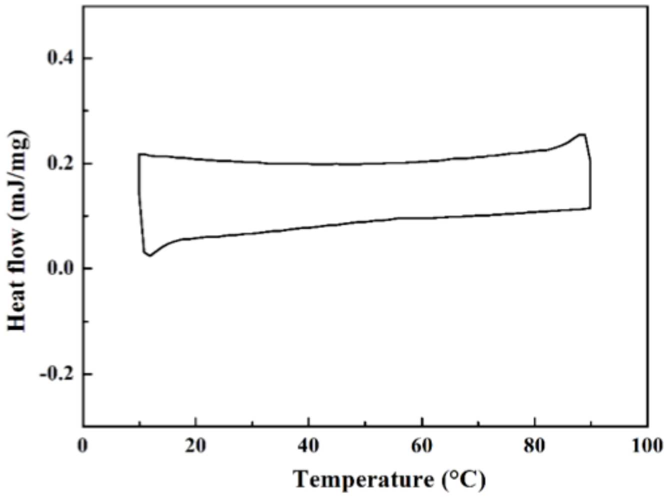

Figure S12 DSC curve of ASF with PEG loading 34%.

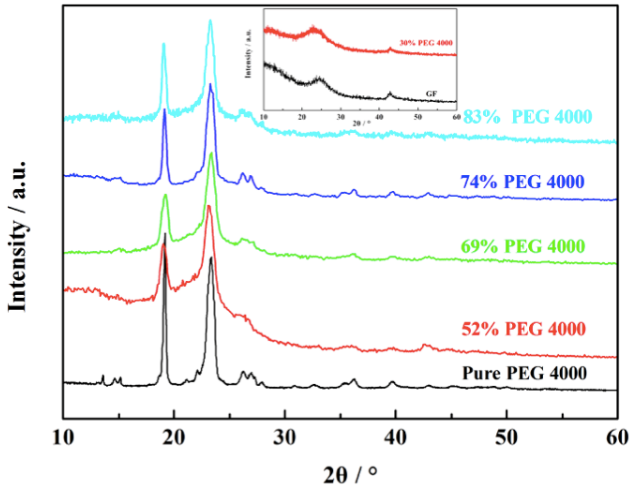

Figure S13 The XRD spectra of pure PEG and ASF with different PEG loading.

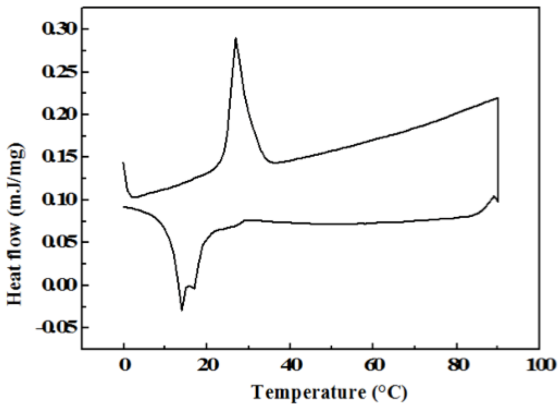

Figure S14 DSC curve of Outlast fiber.

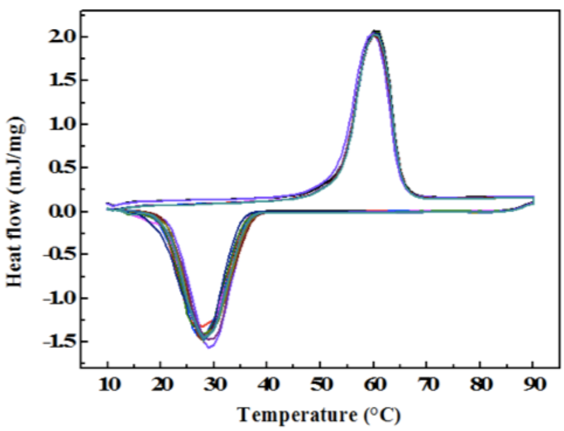

Figure S15 DSC curves of PEG-ASF tested for 20 cycles

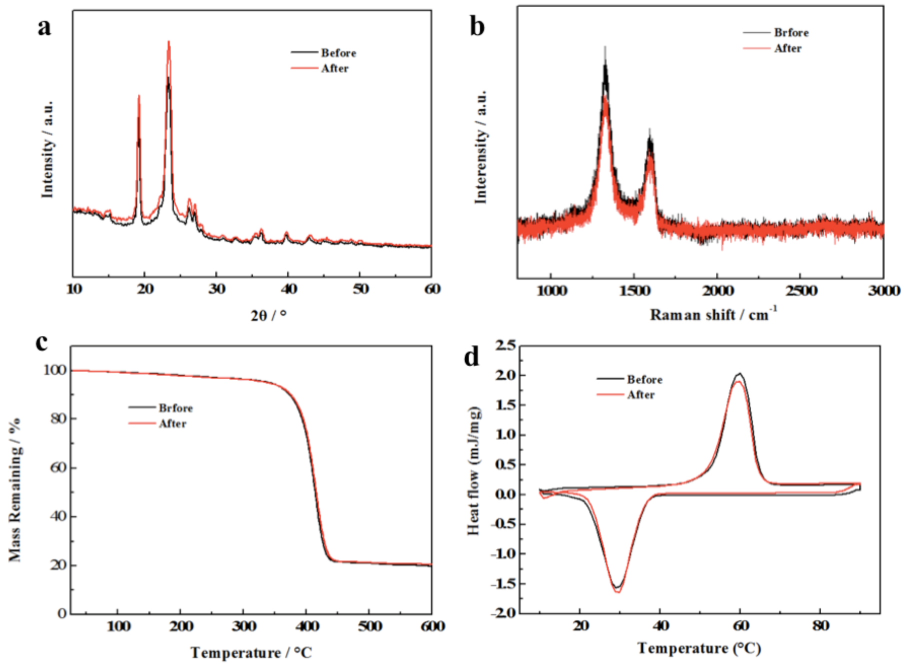

Figure S16 XRD, Raman, TGA and DSC curves of fiber before and after coated by fluonocarbon resin. All curves were virtually identical before and after coating, indicating the FC layer has similar thermal stability when it was coated on ASF, and the enthalpy and phase change behavior was not interfered.

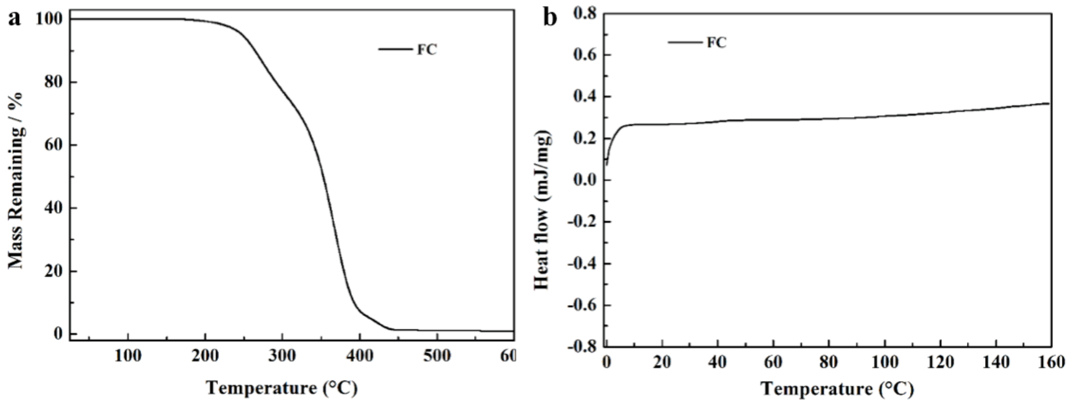

Figure S17 TGA (a) and DSC (b) curves of fluonocarbon resin,

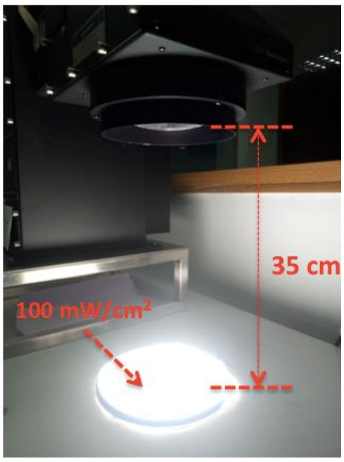

Figure S18 A photograph of solar irradiation.

.

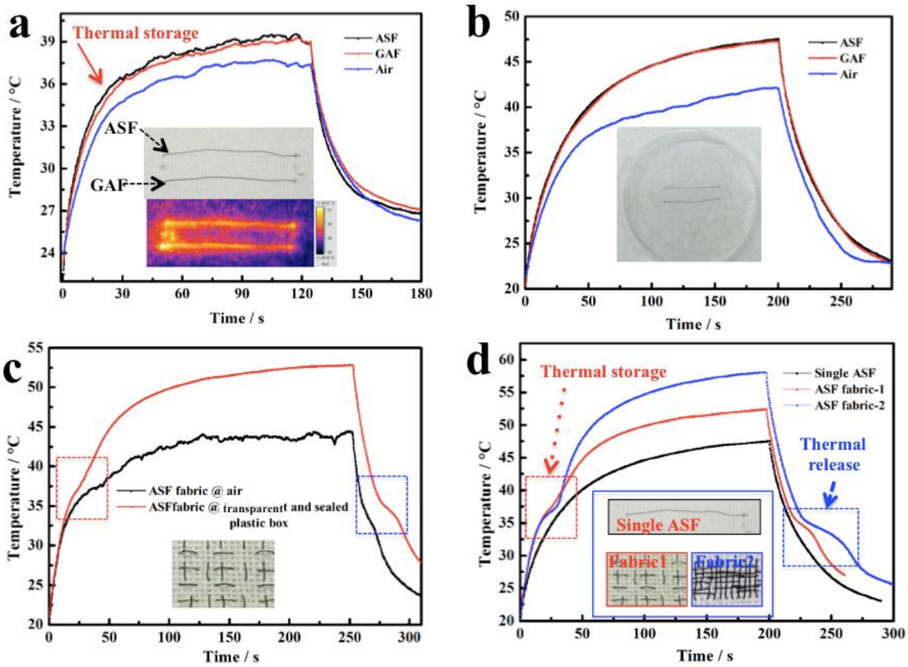

Figure S19 The temperature-time curves of single GAF, ASF in the air (a) and in a transparent/sealed box (b), ASF/cotton fabrics 1 in the air and in a sealed box (c), single ASF, ASF/cotton fabric 1 and 2 in a seal box individually (d) under solar radiation. The inset images are the corresponding photographs and IR image. (ASF-C20. The temperature-time curves were measured and recorded by thermal couple and Keysight 34970 Data Acquisition)

For ASF/cotton fabric 2, under solar irradiation (100 mW/cm^2), the phase change time was about 14.7 s (the plateau of blue curve, and labeled by red point frame), the irradiation surface area (whole fabric) was about 0.75 cm^2, so the received solar energy was about 1102.5 mJ (100*0.75*14.7); the mass of ASF is about 3.6 ± 0.2 mg, the phase change enthalpy was

183.1 J/g, so the storage energy was about 659.16 ± 36.62 mJ; then the thermal energy conversion and storage efficiency was 61.5 ± 1.6%.

All the graphene aerogel and the proposed ASF were a black body which could exhibit ~97% absorption (α, absorptance, *ACS nano* **2018**, *12*, 829), so during the energy conversion process, about 3% energy loss ($\rho+\tau$, reflectance and transmittance) is estimated. During the thermal energy storage process, the energy storage efficiency has been estimated, as mentioned the conversion and storage efficiency was about 61.5 ± 1.6 %, so the energy loss was ~35.5 % (estimated by 97 % - 61.5 %). Details are as follows:

$$Q=Q_\rho+Q_\alpha+Q_\tau$$

$$1=Q_\rho/Q+Q_\alpha/Q+Q_\tau/Q=\rho+\alpha+\tau$$

$$\rho+\tau = 1-\alpha=1-97\% = 3\%$$

——**Equation S1**

Q is the energy of solar irradiation, Q_ρ , the solar energy reflected by ASFs, Q_α , the solar energy absorbed by ASFs, Q_τ , the solar energy transmitted by ASFs, ρ , the reflectance of solar energy, α , the absorptance of solar energy, τ , the transmittance of solar energy.

For the energy release, the released thermal energy is estimated by the freezing phase change enthalpy (ΔH_f = 183.1 J/g) times the mass of ASFs, and the storage thermal energy is estimated by the melting phase change enthalpy (186 J/g) times the mass of ASFs. So the energy loss is the ratio of released energy to stored thermal energy: ~1.5%. The detailed calculation is as follows:

$$\eta_{loss}= (m*\Delta H_f) / (m*\Delta H_m)=183.1 \text{ J/g} /186 \text{ J/g} = \sim 1.5\ \%$$

——**Equation S2**

The comparison of heating effect between ASFs and graphene aerogel fibre (GAF) without PCM were investigated via solar irradiation and electric heating. Under the solar irradiation (Figure S19), we measured and recorded the temperature-time curves of ASF, GAF and the air, no matter the fibres were placed in the air (Figure S19a) or sealed in a transparent box (Figure S19b), the temperature-time profiles of ASF and GAF are almost identical.

Furthermore, the IR images of ASF and GAF showed similar temperature, indicating the graphene fibre was a photo triggered heat generator. Similarly, for the electric heating (Figure S21), the GAF plays a key role for electrically triggered heating according to the IR images. In one word, the GAF plays a role of thermal conversion.

Furthermore，for the temperature-time curves of ASF fabrics under solar irradiation (Figure S19c-d) and electric field (Figure S25a), the temperature plateaus were observed during heating and cooling process, corresponding to the thermal storage and release, respectively, however no temperature plateaus were observed for the GAF (Figure S19d). So the role of PCM is thermal storage.

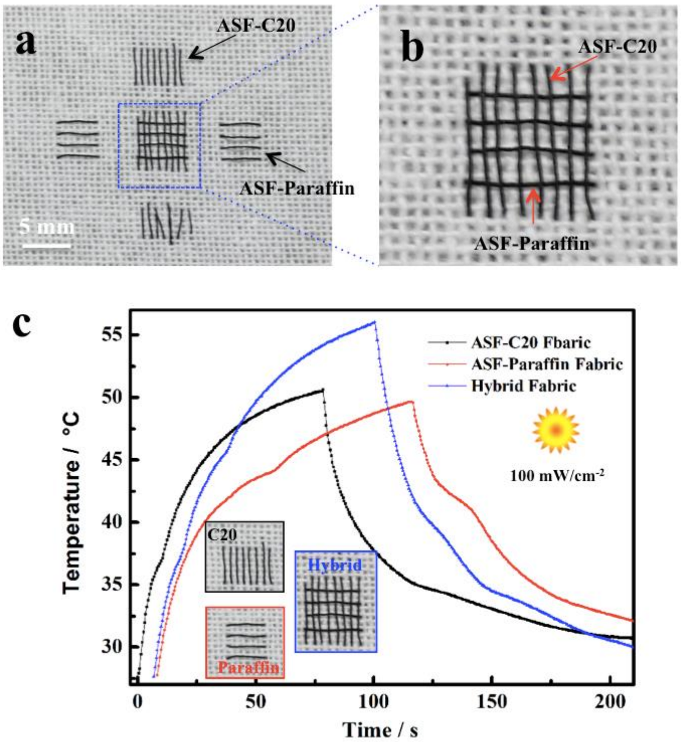

Figure S20 The temperature-time curves (c) of ASF hybrid fabric based on different PCM matrix in a transparent/sealed box. This fabric (a-b) was woven by ASFs with C20 and Paraffin.

When the solar was turn on (t=0), the temperature of ASF hybrid fabrics raised rapidly, and two temperature plateaus occurred under solar irradiation speparately, corresponding to phase transitions of ASF-Paraffin and -C20. When the solar was turn off (t=95s), the temperature dropped, and two temperature hysteresis occurred, corresponding to thermal energy release (phase transition of paraffin and C20). It is very clear that temperature range and capacity of the energy conversion and storage have been enhanced by weaving two types of ASF fibres into a fabic, compared to the single type of fabrics.

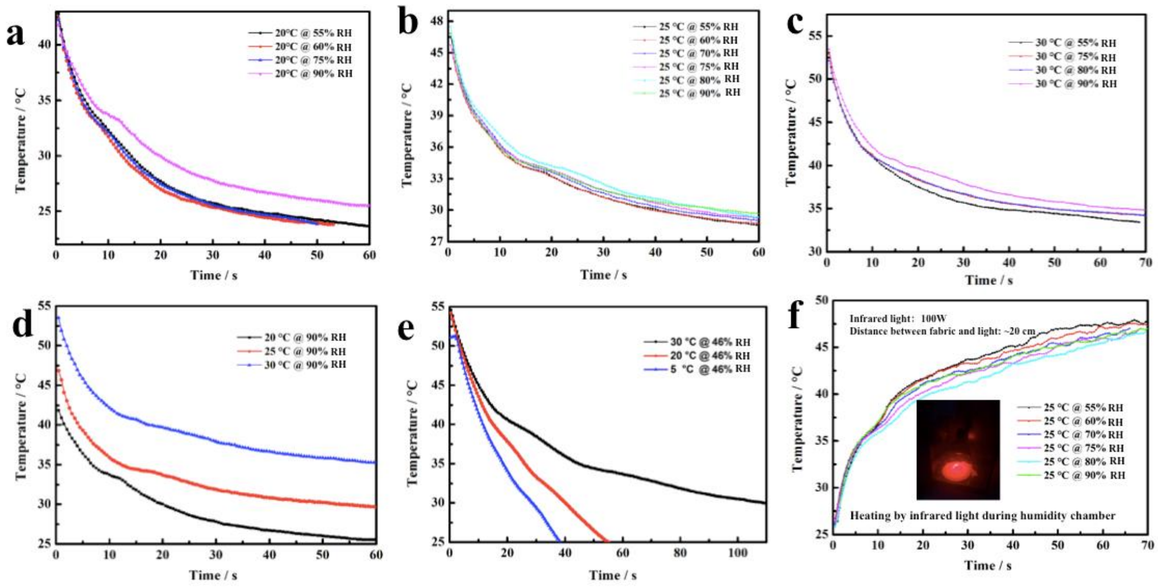

Figure S21 The influence of environment variation on energy release of ASF fabric: The moisture variation at (a) 20 °C, (b) 25 °C, (3) 30 °C. The temperature variation with specific moisture (90%RH) in humidity chamber (d) and that (45%RH) in air (e). The heating process of ASF fabric at 25 °C with different moistures (f). inset in (f) was the heating photograph via infrared light in humidity chamber.

The influence of the moisture on the energy release was weak, mainly attributed to the hydrophobic coating on the ASFs. When the moisture increased rapidly, the energy released speed may slow down slightly (Figure S21a-c and f). The environment temperature affected energy release more significantly. At a lower environment temperature, the enrgy released faster.

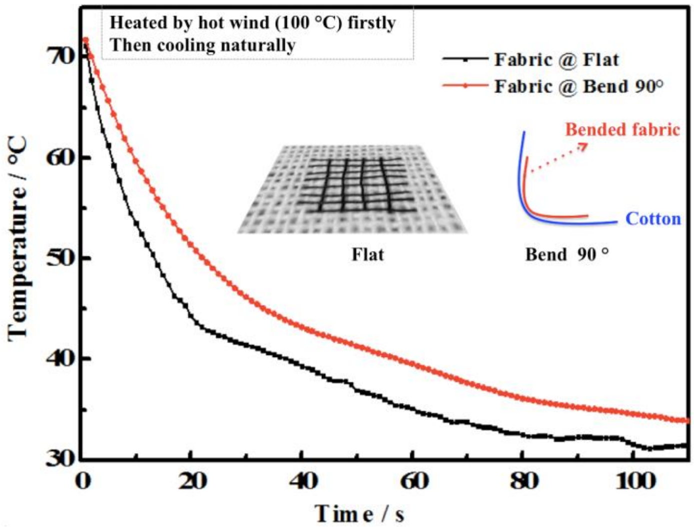

Figure S22 The influence of stress on energy release of the ASF fabric, inset images are the photograph of flat fabric and illustration of Bend.

When the stress makes the fabric bended to ~90 °, as shown in the inset of Figure S22, the released surfaces will close to each other, and the heat dissipation is more confined than that of the flat one, so the energy release slower than that of the flat fabric.

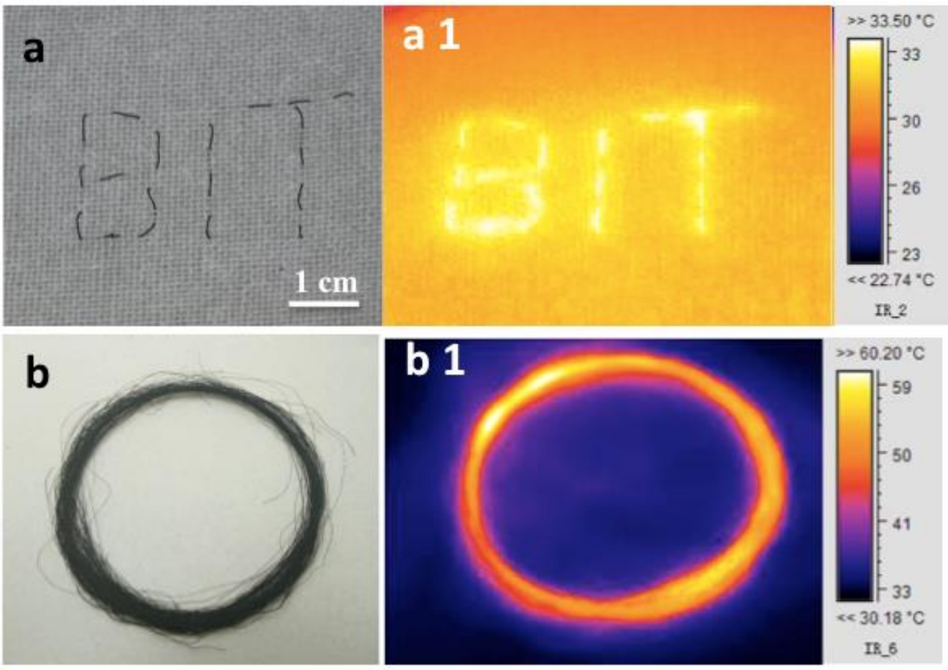

Figure S 23 Photographs and Infrared (IR) images of "BIT" pattern and bundle of ASFs during room temperature (20 °C) under 1.0 sun.

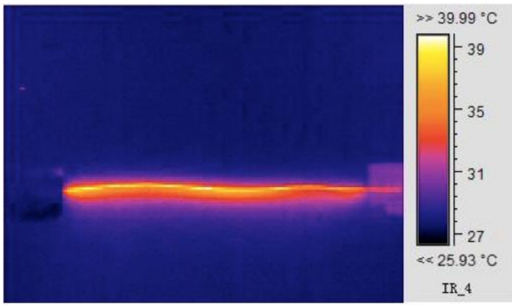

Figure S24 IR image of flat ASF applying an input voltage of 30 V.

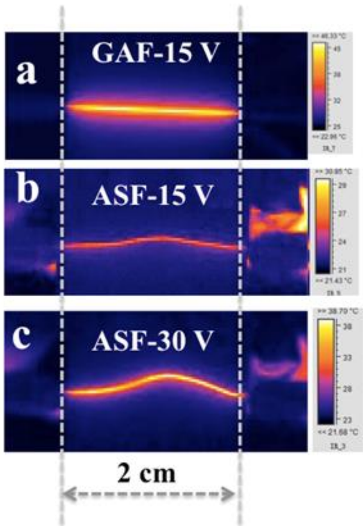

Figure S25 The IR images of single GAF and ASF under different voltages.

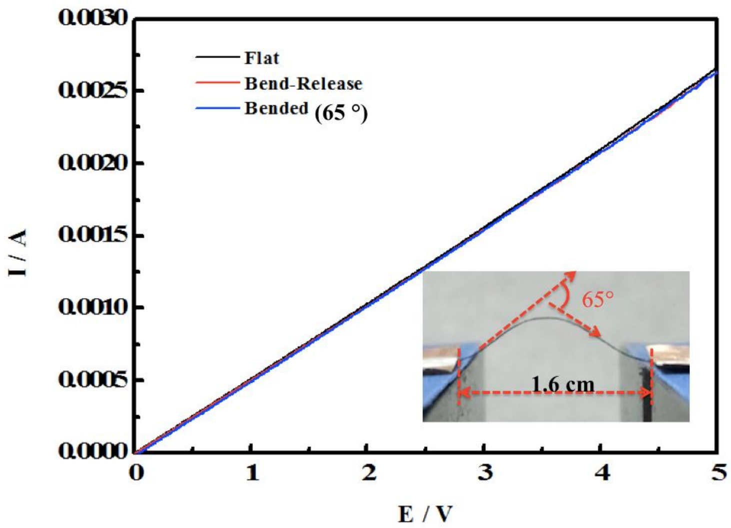

Figure 26 The I-E curves of ASF under different states (flat, bend-release, bended-65°), inset is the corrospending photograph of the bended ASF.

All the I-E curves were coincident, indicating the identical thermal effect, the stable conductive network throughout the PCM matrix, and the excellent thermal exchange interface between graphene and PCM regardless of the different bending conditions.

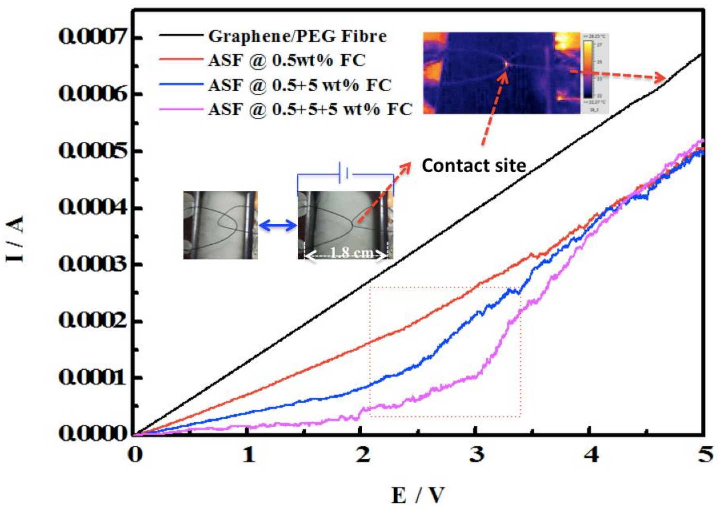

Figure S27 The I-E curves of the cross-touched ASFs with different FC coating thickness.

From 0-5 V, the I-V curve of fibre without FC coating is linearly. After the FC coatings were wrapped on the surface of fibre, the I-V curves will occur a turning point in the scanning voltage range from 2.5 to 3.5V. Before the point, the slopes of curves were small because the FC coating was electrical insulation. After the point, the slope will increase and near to the fibre’s without FC coating. These results claim that the existence of electron tunneling effect.

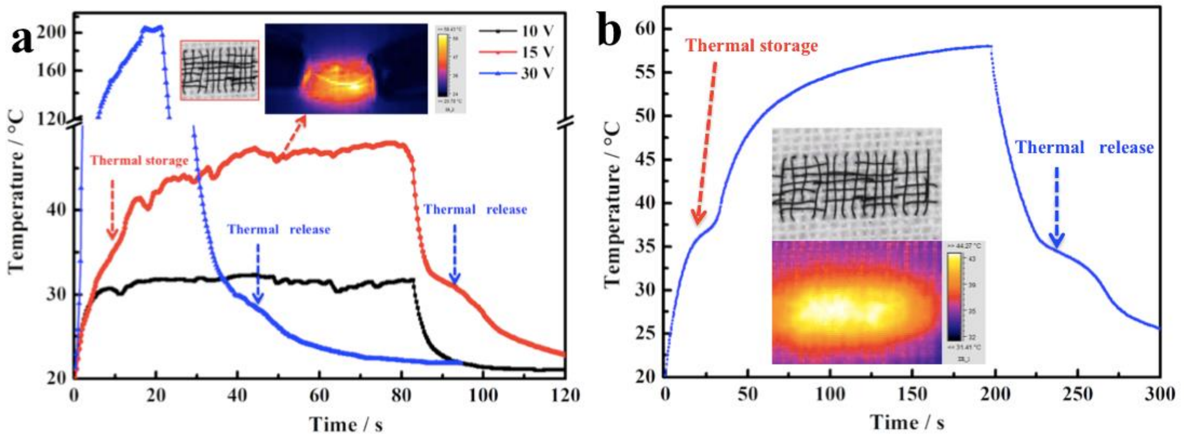

Figure S28 Temperature-time curves of ASF fabric under different voltages (a) and solar irradiation (b). Inset images are the corresponding IR image and photograph.

When the electrical voltage was applied (t=0 s) or the solar was turn on (t=0 s), the heating could be generated by the graphene aerogel skeleton (resistance of graphene aerogel skeleton generate the Joule heating, the black body of graphene aerogel skeleton adsorb the solar energy generate heating), and the PCM was heating and the temperature of the whole ASF increased rapidly, when the temperature reached to about 36 °C, a temperature plateau occurred, corresponding to the solid-liquid phase change transition, until the phase change finished, the temperature will increased again. When the electrical voltage or solar was turn off, the generation of heat stopped, and the temperature will be dropped naturally due to the heat exchange between ASF and environment (about 20 °C), and a temperature plateau (hysteresis) occurred which corresponded to energy release, and the temperature dropped again until the phase change transition finished.

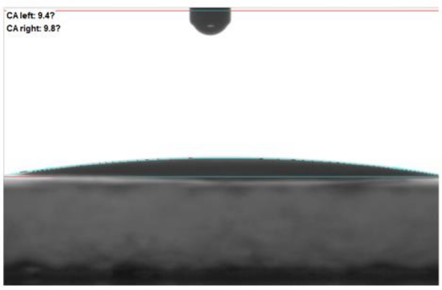

Figure S29 Contact angle of pure PEG.

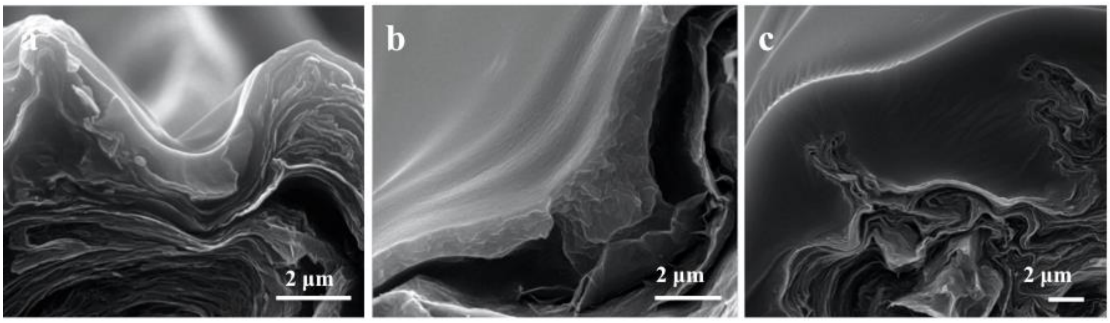

Figure S30 SEM images of PEG-ASFs with different thickness of coating.

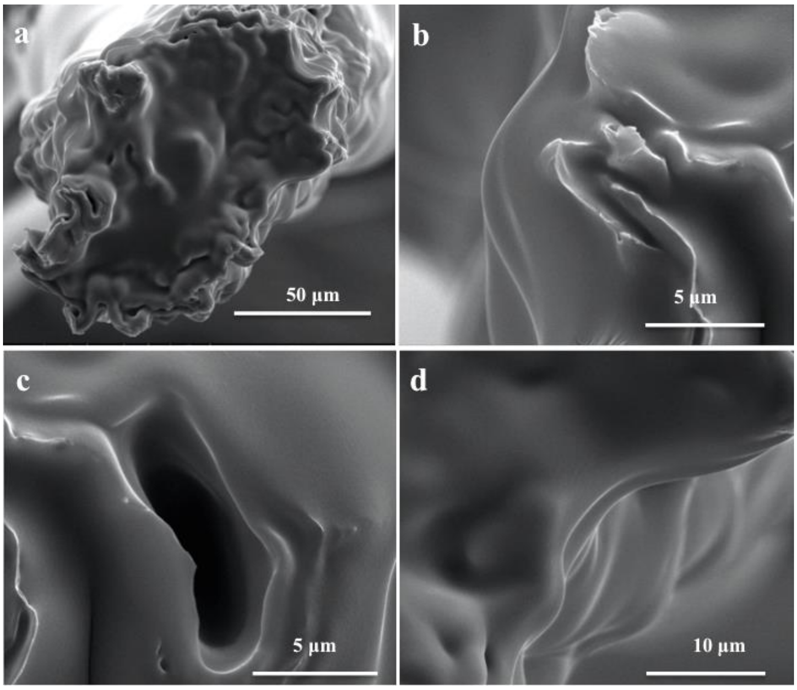

Figure S31 SEM image of the coated cross section of PEG-ASF.

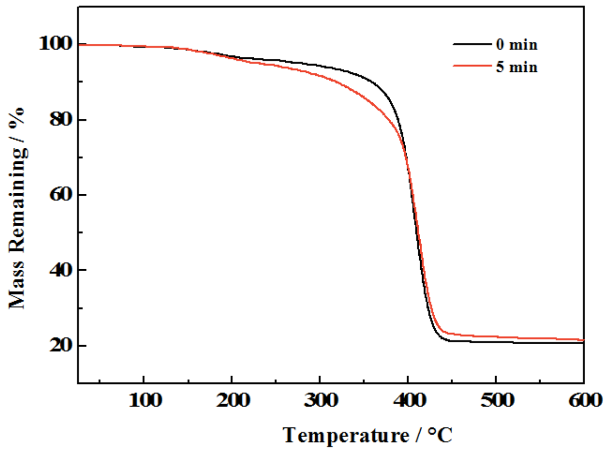

Figure S32 TG curves of graphene/PEG4000 composite fiber before and after washed by water.

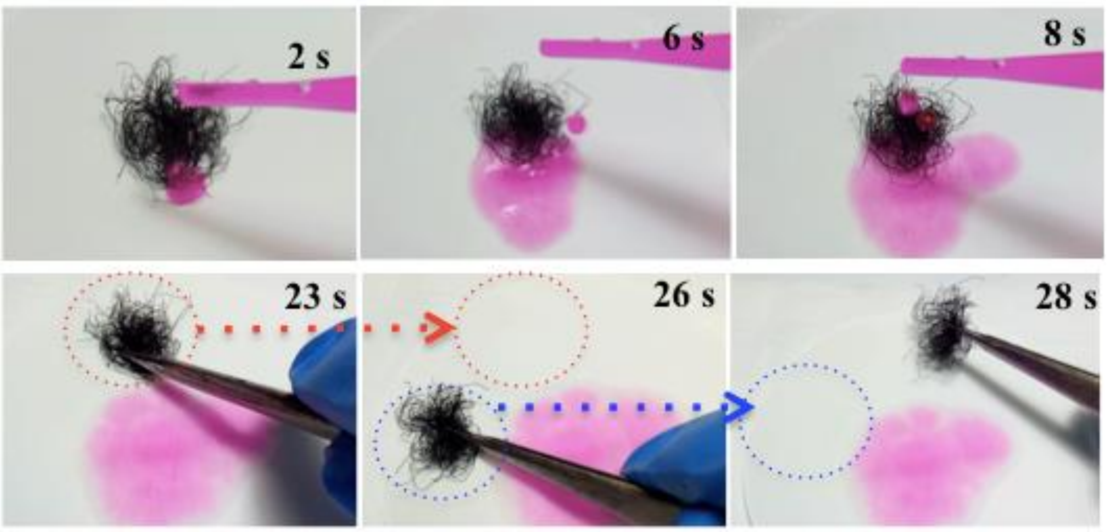

Figure 33 Self-cleaning behavior of ASF mesh.

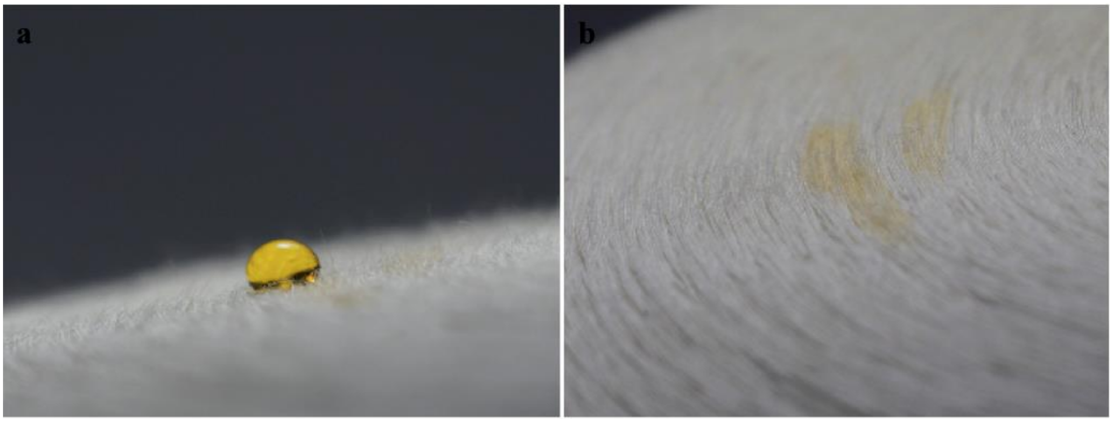

Figure S34 photographs of water droplet on the outlast fiber bundle.

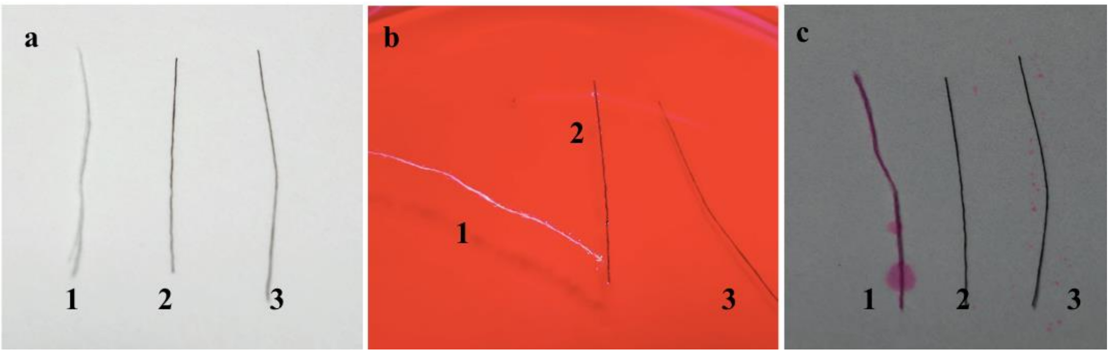

Figure S35 Comparison of self-cleaning function of the Outlast fiber (1), composite fiber (2) and ASF (3).

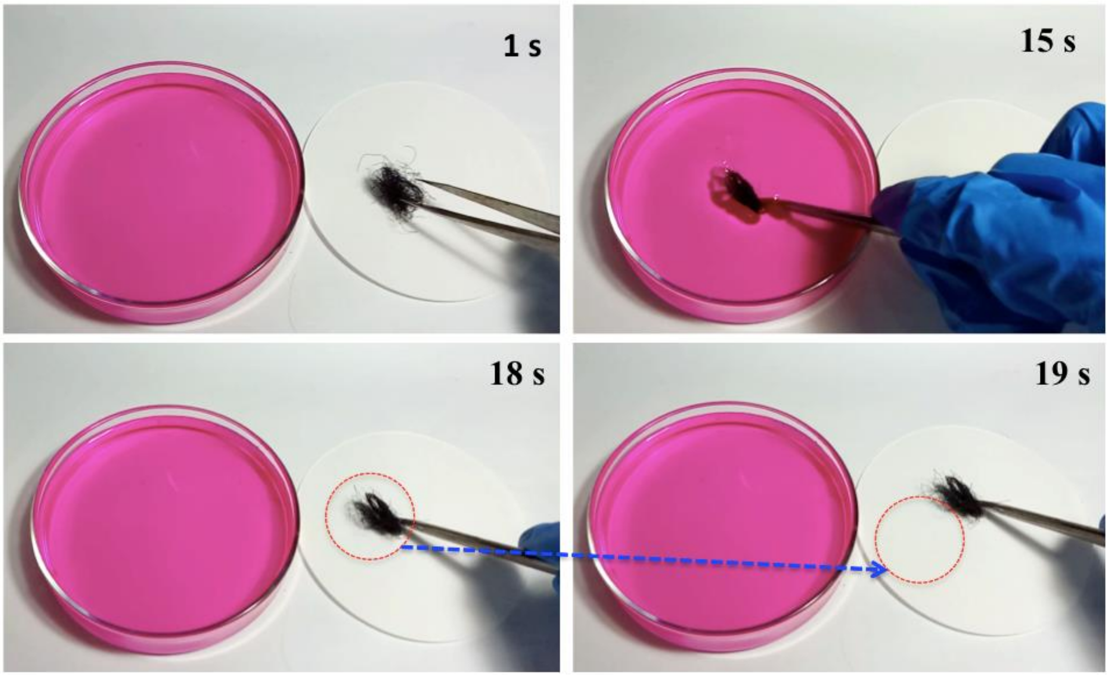

Figure S36 Self-cleaning function of PEG-ASF mesh.

Table:

Table S1 Comparative mechanical data of graphene aerogel-directed smart fibers, commercial outlast fiber and other phase change fibers in previous literatures

Sample [a)]		Diameter (μm)	Enthalpy (J/g)	Electrical conductivity (S/m)	Tensile （MPa）	Specific strength (N/tex)	Young's modulus (GPa)	Specific modulus (N/tex)	Ultimate strain %	Fracture toughness KJ/m^3
This work [b)]	ASF(solid)	184	102	370	12.7	0.0237	1.2	2.24	1.52	82.5
This work [b)]	ASF(melt)	184	102	370	4.98	0.0093	0.11	0.21	5.06	122.4
Commercial	Outlast	20.3	4	EI [c)]	63.7	0.11	0.438	0.756	19.4	6317
Refer. [2]	PVB/Paraffin	~400	128	EI	-	0.00204	-	--	106	-
Refer. [3]	PAN/MES	~0.2	106	EI	0.56	-	-	-	9.83	-
Refer. [4]	polyethylene glycol / cellulose acetate	~2.2	101	EI	5-6	-	-	-	5.5-7	-
Refer. [5]	Lauric acid/polyethylene	~0.5	70.76	EI	4.5	-	-	-	17.2	-
Refer. [6]	Poly(vinyl alcohol)/nonparaffin	~0.75	84.7	EI	2.98	-	-	-	54.5	-

a) The commercial outlast fiber and the phase change fibers references were in the solid state.
b) The ASF used here have a PEG-4000 loading content of 74 wt.%.
c) EI: electrical insulation.

Table S2 Phase change properties of graphene aerogel directed-smart fibers

Sample		Diameter （μm）	Melting process			Freezing process		
			$T_{m,o}$ /°C	$T_{m,p}$ /°C	ΔH_m (J/g)	$T_{f,o}$ /°C	$T_{f,p}$ /°C	ΔH_f (J/g)
PEG4000 Based ASF	100 wt.%	-	57.1	62.7	188.4	38.9	43.3	170.7
	83 wt.%	224.7±7.34	54.3	63.0	116.5	28.9	36.5	105.4
	74 wt.%	183.9±6.22	54.2	60.6	102.8	28.7	33.7	93.7
	69 wt.%	146.9±11.66	50.6	58.0	86.4	25.8	31.1	74.7
	52 wt.%	102.1±5.08	53.7	58.0	28.3	19.1	30.7	16.6
OP44E Based ASF	100 wt.%	-	42.1	50.5	241.3	32.8	34.9	236.6
	85 wt.%	219.2±7.46	40.5	48.9	176.4	35.7	42.1	172.4
C20 Based ASF	100 wt.%	-	36.5	40.3	221	30.4	31.8	214.7
	85 wt.%	231±5.6	36.0	43.9	186	26.9	34.3	183.1
PEG 800 Based ASF	100 wt.%	-	30.0	38.2	127.7	14.4	18.4	125
	85 wt.%	237.1±3.5	28.8	35.4	94.2	7.2	13.0	64.6

References

[1] Y. Yang, R. Zhao, T. Zhang, K. Zhao, P. Xiao, Y. Ma, P. M. Ajayan, G. Shi, Y.Chen, *ACS nano*

2018, *12*, 829.

[2]. G. Q. Wen, R. Xie, W. G. Liang, X. H. He, W. Wang, X. J. Ju, L. Y. Chu, *Appl. Therm. Eng.* **2015**, *87*, 471.

[3]. H. Ke, Z. Pang, Y. Xu, X. Chen, J. Fu, Y. Cai, F. Huang, Q. Wei, *J. Therm. Anal. Calorim.* **2014**, *117*, 109.

[4]. C. Chen，L. Wang，Y. Huang, *Appl. Energy* **2011**, *88*, 3133.

[5]. C. Chen, L. Wang, Y. Huang, *Mater. Lett.* **2008**, *62*, 3515-3517.

[6]. E. Zdraveva，J. Fang，B. Mijovic，T. Lin, *Ind. Eng. Chem. Res.* **2015**, *54*, 8706.

ToC Figure

Click here to access/download
Production Data
Supporting File.docx